The Astrophysical Journal, 754:121 (20pp), 2012 August 1 doi:10.1088/0004-637X/754/2/121

CONSTRAINING THE HIGH-ENERGY EMISSION FROM GAMMA-RAY BURSTS WITH *FERMI*

The *Fermi* Large Area Telescope Team

M. Ackermann[1], M. Ajello[2], L. Baldini[3], G. Barbiellini[4,5], M. G. Baring[6], K. Bechtol[2], R. Bellazzini[3], R. D. Blandford[2], E. D. Bloom[2], E. Bonamente[7,8], A. W. Borgland[2], E. Bottacini[2], A. Bouvier[9], M. Brigida[10,11], R. Buehler[2], S. Buson[12,13], G. A. Caliandro[14], R. A. Cameron[2], C. Cecchi[7,8], E. Charles[2], A. Chekhtman[15,54], J. Chiang[2], S. Ciprini[8,16], R. Claus[2], J. Cohen-Tanugi[17], S. Cutini[16], F. D'Ammando[18,19], F. de Palma[10,11], C. D. Dermer[20], E. do Couto e Silva[2], P. S. Drell[2], A. Drlica-Wagner[2], C. Favuzzi[10,11], Y. Fukazawa[21], P. Fusco[10,11], F. Gargano[11], D. Gasparrini[16], N. Gehrels[22], S. Germani[7,8], N. Giglietto[10,11], F. Giordano[10,11], M. Giroletti[23], T. Glanzman[2], J. Granot[24], I. A. Grenier[25], J. E. Grove[20], D. Hadasch[14], Y. Hanabata[21], A. K. Harding[22], E. Hays[22], D. Horan[26], G. Jóhannesson[27], J. Kataoka[28], J. Knödlseder[29,30], D. Kocevski[2], M. Kuss[3], J. Lande[2], F. Longo[4,5], F. Loparco[10,11], M. N. Lovellette[20], P. Lubrano[7,8], M. N. Mazziotta[11], J. McEnery[22], S. McGlynn[31], P. F. Michelson[2], W. Mitthumsiri[2], M. E. Monzani[2], E. Moretti[32,33], A. Morselli[34], I. V. Moskalenko[2], S. Murgia[2], M. Naumann-Godo[25], J. P. Norris[35], E. Nuss[17], T. Nymark[32,33], T. Ohsugi[36], A. Okumura[2,37], N. Omodei[2], E. Orlando[2,38], J. H. Panetta[2], D. Parent[39,54], V. Pelassa[40], M. Pesce-Rollins[3], F. Piron[17], G. Pivato[13], J. L. Racusin[22], S. Rainò[10,11], R. Rando[12,13], S. Razzaque[39,54], A. Reimer[2,41], O. Reimer[2,41], S. Ritz[9], F. Ryde[32,33], C. Sgrò[3], E. J. Siskind[42], E. Sonbas[22,43,44], G. Spandre[3], P. Spinelli[10,11], M. Stamatikos[22,45], Ëukasz Stawarz[37,46], D. J. Suson[47], H. Takahashi[36], T. Tanaka[2], J. G. Thayer[2], J. B. Thayer[2], L. Tibaldo[12,13], M. Tinivella[3], G. Tosti[7,8], T. Uehara[21], J. Vandenbroucke[2], V. Vasileiou[17], G. Vianello[2,48], V. Vitale[34,49], and A. P. Waite[2]

The *Fermi* Gamma-ray Burst Monitor Team

V. Connaughton[40,53], M. S. Briggs[40,53], S. Guirec[22], A. Goldstein[40], J. M. Burgess[40], P. N. Bhat[40], E. Bissaldi[41], A. Camero-Arranz[44,50], J. Fishman[40], G. Fitzpatrick[51], S. Foley[38,51], D. Gruber[38], P. Jenke[50], R. M. Kippen[52], C. Kouveliotou[50], S. McBreen[38,51], C. Meegan[44], W. S. Paciesas[40], R. Preece[40], A. Rau[38], D. Tierney[51], A. J. van der Horst[50,55], A. von Kienlin[38], C. Wilson-Hodge[50], S. Xiong[40]

[1] Deutsches Elektronen Synchrotron DESY, D-15738 Zeuthen, Germany
[2] W. W. Hansen Experimental Physics Laboratory, Kavli Institute for Particle Astrophysics and Cosmology, Department of Physics and SLAC National Accelerator Laboratory, Stanford University, Stanford, CA 94305, USA; jchiang@slac.stanford.edu, kocevski@slac.stanford.edu
[3] Istituto Nazionale di Fisica Nucleare, Sezione di Pisa, I-56127 Pisa, Italy
[4] Istituto Nazionale di Fisica Nucleare, Sezione di Trieste, I-34127 Trieste, Italy
[5] Dipartimento di Fisica, Università di Trieste, I-34127 Trieste, Italy
[6] Department of Physics and Astronomy, Rice University, MS-108, P.O. Box 1892, Houston, TX 77251, USA
[7] Istituto Nazionale di Fisica Nucleare, Sezione di Perugia, I-06123 Perugia, Italy
[8] Dipartimento di Fisica, Università degli Studi di Perugia, I-06123 Perugia, Italy
[9] Santa Cruz Institute for Particle Physics, Department of Physics and Department of Astronomy and Astrophysics, University of California at Santa Cruz, Santa Cruz, CA 95064, USA
[10] Dipartimento di Fisica "M. Merlin" dell'Università e del Politecnico di Bari, I-70126 Bari, Italy
[11] Istituto Nazionale di Fisica Nucleare, Sezione di Bari, I-70126 Bari, Italy
[12] Istituto Nazionale di Fisica Nucleare, Sezione di Padova, I-35131 Padova, Italy
[13] Dipartimento di Fisica "G. Galilei," Università di Padova, I-35131 Padova, Italy
[14] Institut de Ciències de l'Espai (IEEE-CSIC), Campus UAB, E-08193 Barcelona, Spain
[15] Artep Inc., 2922 Excelsior Springs Court, Ellicott City, MD 21042, USA
[16] Agenzia Spaziale Italiana (ASI) Science Data Center, I-00044 Frascati (Roma), Italy
[17] Laboratoire Univers et Particules de Montpellier, Université Montpellier 2, CNRS/IN2P3, Montpellier, France
[18] IASF Palermo, I-90146 Palermo, Italy
[19] INAF-Istituto di Astrofisica Spaziale e Fisica Cosmica, I-00133 Roma, Italy
[20] Space Science Division, Naval Research Laboratory, Washington, DC 20375-5352, USA
[21] Department of Physical Sciences, Hiroshima University, Higashi-Hiroshima, Hiroshima 739-8526, Japan
[22] NASA Goddard Space Flight Center, Greenbelt, MD 20771, USA
[23] INAF Istituto di Radioastronomia, I-40129 Bologna, Italy
[24] Department of Natural Sciences, The Open University of Israel, 1 University Road, POB 808, Ra'anana 43537, Israel
[25] Laboratoire AIM, CEA-IRFU/CNRS/Université Paris Diderot, Service d'Astrophysique, CEA Saclay, F-91191 Gif sur Yvette, France
[26] Laboratoire Leprince-Ringuet, École polytechnique, CNRS/IN2P3, Palaiseau, France
[27] Science Institute, University of Iceland, IS-107 Reykjavik, Iceland
[28] Research Institute for Science and Engineering, Waseda University, 3-4-1 Okubo, Shinjuku, Tokyo 169-8555, Japan
[29] CNRS, IRAP, F-31028 Toulouse Cedex 4, France
[30] GAHEC, Université de Toulouse, UPS-OMP, IRAP, Toulouse, France
[31] Exzellenzcluster Universe, Technische Universität München, D-85748 Garching, Germany
[32] Department of Physics, Royal Institute of Technology (KTH), AlbaNova, SE-106 91 Stockholm, Sweden; moretti@particle.kth.se
[33] The Oskar Klein Centre for Cosmoparticle Physics, AlbaNova, SE-106 91 Stockholm, Sweden
[34] Istituto Nazionale di Fisica Nucleare, Sezione di Roma "Tor Vergata," I-00133 Roma, Italy
[35] Department of Physics, Boise State University, Boise, ID 83725, USA
[36] Hiroshima Astrophysical Science Center, Hiroshima University, Higashi-Hiroshima, Hiroshima 739-8526, Japan
[37] Institute of Space and Astronautical Science, JAXA, 3-1-1 Yoshinodai, Chuo-ku, Sagamihara, Kanagawa 252-5210, Japan
[38] Max-Planck Institut für Extraterrestrische Physik, D-85748 Garching, Germany
[39] Center for Earth Observing and Space Research, College of Science, George Mason University, Fairfax, VA 22030, USA
[40] Center for Space Plasma and Aeronomic Research (CSPAR), University of Alabama in Huntsville, Huntsville, AL 35899, USA; connauv@uah.edu, valerie@nasa.gov, michael.briggs@nasa.gov

[41] Institut für Astro- und Teilchenphysik and Institut für Theoretische Physik, Leopold-Franzens-Universität Innsbruck, A-6020 Innsbruck, Austria
[42] NYCB Real-Time Computing Inc., Lattingtown, NY 11560-1025, USA
[43] Department of Physics, Adıyaman University, 02040 Adıyaman, Turkey
[44] Universities Space Research Association (USRA), Columbia, MD 21044, USA
[45] Department of Physics, Center for Cosmology and Astro-Particle Physics, The Ohio State University, Columbus, OH 43210, USA
[46] Astronomical Observatory, Jagiellonian University, 30-244 Kraków, Poland
[47] Department of Chemistry and Physics, Purdue University Calumet, Hammond, IN 46323-2094, USA
[48] Consorzio Interuniversitario per la Fisica Spaziale (CIFS), I-10133 Torino, Italy
[49] Dipartimento di Fisica, Università di Roma "Tor Vergata," I-00133 Roma, Italy
[50] NASA Marshall Space Flight Center, Huntsville, AL 35812, USA
[51] University College Dublin, Belfield, Dublin 4, Ireland
[52] Los Alamos National Laboratory, Los Alamos, NM 87545, USA
[53] Physics Department, University of Alabama in Huntsville, Huntsville, AL 35899, USA
Received 2011 December 16; accepted 2012 May 22; published 2012 July 17

ABSTRACT

We examine 288 gamma-ray bursts (GRBs) detected by the *Fermi Gamma-ray Space Telescope*'s Gamma-ray Burst Monitor (GBM) that fell within the field of view of *Fermi*'s Large Area Telescope (LAT) during the first 2.5 years of observations, which showed no evidence for emission above 100 MeV. We report the photon flux upper limits in the 0.1–10 GeV range during the prompt emission phase as well as for fixed 30 s and 100 s integrations starting from the trigger time for each burst. We compare these limits with the fluxes that would be expected from extrapolations of spectral fits presented in the first GBM spectral catalog and infer that roughly half of the GBM-detected bursts either require spectral breaks between the GBM and LAT energy bands or have intrinsically steeper spectra above the peak of the νF_ν spectra ($E_{\rm pk}$). In order to distinguish between these two scenarios, we perform joint GBM and LAT spectral fits to the 30 brightest GBM-detected bursts and find that a majority of these bursts are indeed softer above $E_{\rm pk}$ than would be inferred from fitting the GBM data alone. Approximately 20% of this spectroscopic subsample show statistically significant evidence for a cutoff in their high-energy spectra, which if assumed to be due to $\gamma\gamma$ attenuation, places limits on the maximum Lorentz factor associated with the relativistic outflow producing this emission. All of these latter bursts have maximum Lorentz factor estimates that are well below the minimum Lorentz factors calculated for LAT-detected GRBs, revealing a wide distribution in the bulk Lorentz factor of GRB outflows and indicating that LAT-detected bursts may represent the high end of this distribution.

Key words: gamma-ray burst: general – gamma rays: general

Online-only material: color figures

1. INTRODUCTION

Observations by the *Fermi Gamma-ray Space Telescope* have dramatically increased our knowledge of the broadband spectra of gamma-ray bursts (GRBs). The Gamma-ray Burst Monitor (GBM) on board *Fermi* has detected over 700 GRBs in roughly 3 years of triggered operations. Of these bursts, 29 have been detected at energies > 100 MeV by *Fermi*'s Large Area Telescope (LAT); and five of these bursts, GRB 080916C, GRB 090510, GRB 090328, GRB 090902B, and GRB 090926A, have been detected at energies > 10 GeV. The high-energy emission from the majority of these bursts show evidence for being consistent with the high-energy component of the smoothly joined broken power law, commonly referred to as the Band spectrum (Band et al. 1993), that has been observed in the GBM energy range. Three of these bursts, GRB 090510 (Ackermann et al. 2010), GRB 090902B (Abdo et al. 2009a), and GRB 090926A (Ackermann et al. 2011), though, exhibit an additional hard spectral component that is distinct from the continuum emission observed at sub-MeV energies.

Similar high-energy emission above 100 MeV was detected by the Energetic Gamma-Ray Experiment Telescope (EGRET) on board the *Compton Gamma-Ray Observatory* and by the *AGILE* spacecraft (Del Monte et al. 2011). The prompt high-energy emission detected by EGRET from GRB 930131 (Sommer et al. 1994; Kouveliotou et al. 1994) and GRB 940217 (Hurley et al. 1994) was consistent with an extrapolation of the GRB spectrum as measured by the Burst And Transient Source Experiment (BATSE) in the 25 keV–2 MeV energy range. EGRET observations of GRB 941017 (González et al. 2003), on the other hand, showed evidence for an additional hard spectral component that extended up to 200 MeV, the first such detection in a GRB spectrum.

Unlike these previous detections by EGRET, many of the LAT-detected bursts have measured redshifts, made possible through X-ray localizations by the *Swift* spacecraft (Gehrels et al. 2004) and ground-based follow-up observations of their long-lived afterglow emission. The high-energy detections, combined with the redshift to these GRBs, have shed new light into the underlying physics of this emission. At a redshift of $z = 0.903$ (McBreen et al. 2010), the detection of GeV photons from GRB 090510 indicates a minimum bulk Lorentz factor of $\Gamma_{\gamma\gamma,\rm min} \sim 1200$ in order for the observed gamma rays to have avoided attenuation due to electron–positron pair production (Ackermann et al. 2010). Furthermore, a spectral cutoff at $\sim$1.4 GeV is quite evident in the high-energy component of GRB 090926A, which, if interpreted as opacity due to $\gamma\gamma$ attenuation within the emitting region, allows for a direct estimate of the bulk Lorentz factor of $\Gamma \sim 200$–700 for the outflow producing the emission (Ackermann et al. 2011).

Perhaps equally important for unraveling the nature of the prompt emission is the lack of a significant detection above 100 MeV for the majority of the GRBs detected by the GBM. The LAT instrument has detected roughly 8% of the GBM-triggered GRBs that have occurred within the LAT

[54] Resident at Naval Research Laboratory, Washington, DC 20375, USA.
[55] NASA Postdoctoral Program Fellow, USA.

field of view (FOV). This detection rate places limits on the ubiquity of the extra high-energy components detected by LAT, EGRET, and *AGILE*. Such a component would be a natural consequence of synchrotron emission from relativistic electrons in an internal shock scenario, but, for example, might be suppressed in Poynting flux-dominated models (e.g., see Fan & Piran 2008). Therefore, a systematic analysis of the non-detections of high-energy components in GBM-detected GRBs may significantly help to discriminate between various prompt emission mechanisms. Furthermore, the lack of a detection by the LAT of GBM-detected GRBs with particularly hard spectra points to intrinsic spectral cutoffs and/or curvature at high energies, giving us further insight into the physical properties of the emitting region.

In this paper, we examine the GBM-detected bursts that fell within the LAT FOV at the time of trigger during the first 2.5 years of observations which showed no evidence for emission above 100 MeV. We report the photon flux upper limits in the 0.1–10 GeV band during the prompt emission phase and for 30 s and 100 s integrations starting from the trigger time for each burst. We then compare these upper limits with the fluxes that would be expected from extrapolations of spectral fits presented in the first GBM spectral catalog (Goldstein et al., 2012) in order to determine how well measurements of the $\lesssim$MeV properties of GRBs can predict detections at >100 MeV energies.

We find that roughly half of the GBM-detected bursts either require spectral breaks or have intrinsically steeper spectra in order to explain their non-detections by the LAT. We distinguish between these two scenarios by performing joint GBM and LAT spectral fits to a subset of the 30 brightest bursts, as seen by the GBM that were simultaneously in the LAT FOV. We find that while a majority of these bursts have spectra that are softer above the peak of the νF_ν spectra ($E_{\rm pk}$) than would be inferred from fitting the GBM data alone, a subset of bright bursts have a statistically significant high-energy spectral cutoff similar to the spectral break reported for GRB 090926A (Ackermann et al. 2011). These results are consistent with those presented by Beniamini et al. (2011) and Guetta et al. (2011) who perform a variation of the upper limit analysis presented here on a smaller sample of GBM-detected bursts. Finally, we use our joint GBM and LAT spectral fits in conjunction with the LAT non-detections at 100 MeV to place limits on the maximum Lorentz factor for these GRBs that show evidence for intrinsic spectral breaks.

The paper is structured as follows: in Section 2, we review the characteristics of the GBM and LAT instruments, and in Section 3, we define the GRB samples considered in this work. In Section 4, we describe the analysis we perform to quantify the significance of the LAT non-detections; we present the results in Section 5, and discuss the implications they have on our understanding of the properties associated with the prompt gamma-ray emission in Section 6.

2. THE LAT AND GBM INSTRUMENTS

The *Fermi Gamma-ray Space Telescope* carries the Gamma-ray Burst Monitor (Meegan et al. 2009) and the Large Area Telescope (Atwood et al. 2009). The GBM has 14 scintillation detectors that together view the entire unocculted sky. Triggering and localization are performed using 12 sodium iodide (NaI) and 2 bismuth germanate (BGO) detectors with different orientations placed around the spacecraft. The two BGO scintillators are placed on opposite sides of the spacecraft so that at least one detector is in view for any direction on the sky. GBM spectroscopy uses both the NaI and BGO detectors, sensitive between 8 keV and 1 MeV, and 150 keV and 40 MeV, respectively, so that their combination provides an unprecedented four decades of energy coverage with which to perform spectroscopic studies of GRBs.

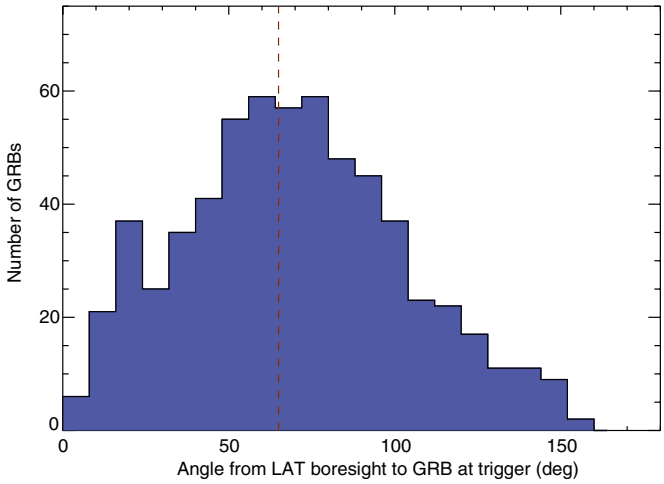

Figure 1. Distribution of LAT off-axis angles of the 620 bursts that triggered the GBM from 2008 August 4 to 2011 January 1. The red dashed line at an off-axis angle of 65° indicates the nominal boundary of the LAT FOV. A total of 288 bursts (46% of all detected bursts) fell within the LAT FOV over this period.

(A color version of this figure is available in the online journal.)

The LAT is a pair conversion telescope comprising a 4×4 array of silicon strip trackers and cesium iodide (CsI) calorimeters covered by a segmented anti-coincidence detector (ACD) to reject charged-particle background events. The LAT covers the energy range from 20 MeV to more than 300 GeV with an FOV of $\sim$2.4 sr. The dead time per event of the LAT is nominally 26.50 μs for most events, although about 10% of the event readouts include more calibration data, which engender longer dead times. This dead time is four orders of magnitude shorter than that of EGRET. This is crucial for observations of high-intensity transient events such as GRBs. The LAT triggers on many more background events than celestial gamma rays. Onboard background rejection is supplemented on the ground using event class selections that accommodate the broad range of sources of interest.

3. SAMPLE DEFINITION

We compiled a sample of all GRBs detected by the GBM between the beginning of normal science operations of the *Fermi* mission on 2008 August 4 up to 2011 January 1, yielding a total of 620 GRBs. Of these, 288 bursts fell within 65° of the LAT z-axis (or boresight) at the time of GBM trigger, which we define as the LAT FOV. Bursts detected at angles greater than 65° at the time of the GBM trigger were not considered for this analysis, due to the greatly reduced sensitivity of the instrument for such large off-axis angles. A plot of the distribution of the LAT boresight angles at trigger time, T_0, for all 620 bursts is shown in Figure 1. Roughly half (46%) of the GBM-detected GRBs fell within the LAT FOV at T_0, as expected given the relative sky coverage of the two instruments. These bursts make up the sample for which the photon flux upper limits described in the next section have been calculated. A complete list of the 288 bursts in the sample, their positions, their durations, and their LAT boresight angles is given in Table 1.

Table 1
Burst Sample with Select Parameters

GRB Index	MET[a] (s)	R.A. (°)	Decl. (°)	Error (°)	Angle[b] (°)	T100 (s)	$F_{\rm lim,T100}$	$F_{\rm lim,30\,s}$	$F_{\rm lim,100\,s}$
							($\times 10^{-5}$ photons cm^{-2} s^{-1})		
080804972	239584816	328.70	−53.20	0.0	56.4	22.0	7.1	5.3	1.7
080805496	239630032	322.70	47.90	5.6	13.0	28.0	...	2.3	0.8
080806896	239750976	241.80	46.70	2.9	59.6	44.0	8.4	12.4	4.0
080808565	239895232	33.60	5.40	2.6	57.9	18.0	10.5	8.1	2.3
080808772	239913104	96.70	−14.40	12.3	17.0	1.0	65.5	2.3	1.4
080810549	240066608	356.80	0.32	0.0	60.8	53.0	4.0	6.9	2.3
080816503	240581056	156.20	42.60	2.0	59.1	68.0	2.7	6.0	2.9
080824909	241307328	122.40	−2.80	1.0	18.1	10.0	7.6	4.6	1.9
080825593	241366432	232.20	−4.90	1.0	60.0	35.0	31.5	34.0	12.6
080830368	241779024	160.10	30.80	2.5	23.5	47.0	1.9	2.4	1.2
080904886	242255760	214.20	−30.30	2.1	21.8	18.0	4.2	3.3	0.9
080905499	242308736	287.70	−18.90	0.0	27.9	1.0	71.1	6.3	2.2
080906212	242370320	182.80	−6.40	1.3	34.9	3.0	60.7	3.9	1.6
080912360	242901536	25.80	−7.20	7.1	57.8	8.0	24.0	5.8	2.1
080916009	243216768	119.80	−56.60	0.0	48.8	86.0	76.7	171.8	68.6
080920268	243584752	121.60	8.90	5.4	21.0	1.0	79.9	4.9	1.2
080924766	243973360	72.80	32.50	4.4	60.1	17.0	12.0	6.2	2.1
080925775	244060560	96.10	18.20	1.2	38.0	33.0	6.0	6.6	2.7
080928628	244307104	95.10	−55.20	0.0	39.4	12.0	7.4	3.0	1.0
081003644	244740432	259.10	35.40	6.9	62.7	147.0	10.6	11.3	6.9
081006604	244996176	142.00	−67.40	8.0	16.0	144.0	1.2	3.4	0.9
081006872	245019344	172.20	−61.00	8.7	16.0	1.0	71.1	3.8	1.5
081008832	245188688	280.00	−57.40	0.0	64.2	126.0	6.2	9.6	5.9
081012549	245509824	30.20	−17.60	0.0	61.5	7.0	31.9	6.6	1.7
081024891	246576160	322.90	21.20	0.0	18.6	134.0	1.0	8.8	2.6
081101491	247232800	95.10	−0.10	0.0	29.9	1.0	71.9	3.5	1.1
081102365	247308304	225.30	22.00	8.6	61.0	147.0	2.2	6.7	2.0
081102739	247340656	331.20	53.00	0.0	50.9	41.0	3.3	4.6	2.3
081107321	247736528	51.00	17.10	3.5	52.0	3.0	60.1	4.9	2.0
081115891	248476944	190.60	63.30	15.1	53.0	1.0	131.4	4.7	2.5
081118876	248734848	54.60	−43.30	3.6	34.1	23.0	3.4	2.6	1.1
081122520	249049696	339.10	40.00	1.0	19.2	25.0	6.1	4.7	1.0
081122614	249057808	151.40	−2.10	11.2	52.0	1.0	120.7	4.2	1.2
081126899	249428048	323.50	48.70	0.0	17.5	8.0	10.2	4.0	2.8
081204004	250041920	63.30	−62.60	4.8	57.0	3.0	77.2	5.5	2.7
081207680	250359520	112.40	70.50	1.2	60.2	101.0	8.2	11.0	5.1
081213173	250834176	12.90	−33.90	13.2	55.0	1.0	145.8	6.2	2.1
081217983	251249696	116.80	26.80	2.0	53.5	24.0	7.6	6.2	1.9
081222204	251614448	22.70	−34.10	0.0	50.0	45.0	5.9	9.2	2.7
081223419	251719440	112.50	33.20	3.8	30.0	3.0	37.6	4.5	1.1
081224887	251846272	201.70	75.10	1.0	17.9	35.0	4.7	5.1	2.3
081225257	251878160	234.10	−64.60	6.9	46.4	15.0	21.3	10.6	5.3
081226156	251955888	193.00	26.80	2.4	51.8	11.0	13.3	4.7	1.6
081226509	251986384	25.50	−47.40	0.0	22.5	1.0	75.3	2.8	1.2
081229187	252217744	172.60	56.90	8.8	44.0	1.0	86.6	2.9	0.9
081230871	252363216	207.60	−17.30	7.7	23.0	1.0	69.6	2.4	0.9
081231140	252386464	208.60	−35.80	1.0	23.3	36.0	2.1	2.5	0.8
090112332	253439840	110.90	−30.40	1.0	4.1	52.0	1.6	3.1	1.1
090113778	253564848	32.10	33.40	0.0	31.2	9.0	9.2	4.2	1.1
090117335	253872128	227.30	−41.50	4.8	63.6	3.0	117.9	9.7	3.5
090117632	253897840	121.60	−38.80	1.9	57.7	27.0	6.0	5.3	1.7
090117640	253898528	164.00	−58.20	0.0	50.9	148.0	3.7	6.8	3.4
090126227	254640384	189.20	34.10	3.6	19.0	7.0	11.0	2.5	1.3
090129880	254956032	269.00	−32.80	0.0	24.4	16.0	7.1	3.5	1.0
090131090	255060560	352.30	21.20	1.0	42.2	55.0	2.4	3.0	1.2
090202347	255255568	274.30	−2.00	2.6	57.0	15.0	12.1	6.0	2.0
090207777	255724752	252.70	34.90	3.8	46.9	14.0	9.6	5.0	1.5
090213236	256196368	330.60	−55.00	3.1	19.2	1.0	67.8	4.7	1.5
090217206	256539408	204.90	−8.40	0.0	34.5	37.0	15.4	19.1	6.9
090227310	257412352	3.30	−43.00	1.2	21.3	15.0	6.2	4.0	2.5
090228204	257489600	106.80	−24.30	1.0	16.0	1.0	68.2	2.5	0.7
090228976	257556304	357.60	36.70	3.3	21.2	5.0	16.8	2.5	1.1
090301315	257585616	352.80	9.50	5.0	54.0	4.0	43.2	4.9	1.5
090303542	257778032	223.70	−68.20	12.1	26.0	1.0	63.2	2.5	1.4
090304216	257836256	195.90	−73.40	12.3	42.0	1.0	94.7	3.3	1.9

Table 1
(Continued)

GRB Index	MET[a] (s)	R.A. (°)	Decl. (°)	Error (°)	Angle[b] (°)	T100 (s)	$F_{\rm lim,T100}$	$F_{\rm lim,30\,s}$	$F_{\rm lim,100\,s}$
							($\times 10^{-5}$ photons cm^{-2} s^{-1})		
090305052	257908480	135.00	74.30	5.4	37.0	2.0	81.5	3.0	1.9
090306245	258011520	137.00	57.00	4.1	17.0	20.0	3.5	2.5	1.0
090308734	258226592	21.90	−54.30	4.8	50.0	1.0	111.2	8.0	2.2
090309767	258315904	174.30	−49.50	3.6	36.1	16.0	7.4	3.6	1.0
090319622	259167344	283.30	−8.90	2.6	17.9	37.0	2.4	3.0	0.9
090320045	259203920	108.30	−43.30	17.9	40.0	1.0	84.8	3.8	1.3
090320418	259236112	238.00	−46.50	12.0	61.0	1.0	194.8	17.3	5.9
090323002	259459360	190.70	17.10	0.0	57.2	144.0	6.9	14.8	9.1
090328401	259925808	90.90	−42.00	0.0	64.5	85.0	13.1	17.0	11.0
090330279	260088144	160.20	−8.20	2.1	51.4	27.0	6.3	5.7	2.1
090331681	260209216	210.50	3.10	9.3	41.0	1.0	83.9	3.1	1.4
090403314	260436768	67.10	47.20	9.7	42.1	14.0	7.6	5.0	1.8
090411838	261173200	156.00	−68.90	2.1	60.3	17.0	17.9	12.5	5.2
090413122	261284160	266.50	−9.20	5.5	50.8	12.0	23.7	7.4	2.1
090418816	261776128	262.80	−28.20	14.4	57.9	1.0	165.2	11.4	2.7
090419997	261878112	88.60	31.30	3.6	55.8	87.0	2.4	5.6	2.1
090422150	262064112	294.70	40.40	0.0	29.2	1.0	76.3	3.8	1.1
090426066	262402544	17.60	−19.20	18.1	56.0	1.0	149.8	5.2	1.8
090427644	262538816	210.00	−45.70	11.8	14.0	1.0	96.8	4.7	1.0
090429753	262721040	124.40	7.90	5.0	32.0	2.0	73.2	2.5	1.5
090510016	263607776	333.60	−26.60	0.0	13.6	1.0	1626.0	143.3	43.7
090514006	263952528	12.30	−10.90	4.6	17.0	44.0	2.3	2.3	1.2
090516137	264136640	122.20	−71.62	2.6	47.8	147.0	1.7	5.7	1.8
090516353	264155280	138.26	−11.85	0.0	19.3	85.0	1.3	2.7	1.1
090518080	264304480	119.95	0.75	0.0	36.8	1.0	78.3	3.2	1.4
090519462	264423936	119.00	−46.30	7.2	31.0	2.0	77.7	3.0	2.5
090519881	264460128	142.30	0.20	0.0	47.5	18.0	6.2	3.7	1.5
090520832	264542272	332.00	43.20	12.0	10.0	1.0	61.1	2.8	0.9
090522344	264672944	277.70	19.60	4.9	55.1	3.0	70.8	4.5	...
090524346	264845872	327.30	−66.90	1.5	62.3	55.0	4.2	8.5	2.4
090529310	265274784	231.20	32.20	7.2	39.0	147.0	1.0	3.2	1.0
090531775	265487760	252.06	−36.05	0.0	21.9	2.0	101.3	5.7	1.8
090612619	266511056	81.03	17.71	2.2	54.1	6.0	33.6	6.1	2.6
090617208	266907600	78.89	15.65	4.2	45.0	2.0	113.5	3.5	1.0
090620400	267183392	237.35	61.15	1.0	56.0	21.0	14.4	9.9	3.6
090621185	267251200	11.02	61.94	0.0	10.9	48.0	1.8	3.3	1.0
090621417	267271248	257.49	−28.46	3.2	52.6	36.0	4.1	5.1	1.4
090623913	267486864	41.70	1.80	1.5	36.8	7.0	11.7	2.6	1.3
090625234	267601024	20.29	−6.43	3.1	13.8	13.0	5.3	2.6	0.7
090626189	267683536	169.30	−36.05	1.0	18.3	79.0	3.7	3.3	4.2
090629543	267973280	8.48	17.67	7.4	40.0	1.0	96.8	3.6	1.7
090701225	268118640	114.69	−42.07	4.2	12.0	1.0	65.5	2.5	1.7
090703329	268300448	3.30	6.90	6.6	22.0	5.0	26.1	4.1	1.4
090704783	268426016	312.97	20.43	16.5	34.5	16.0	5.3	2.8	1.2
090706283	268555648	205.07	−47.07	3.0	20.8	86.0	1.5	3.4	1.3
090708152	268717088	154.63	26.64	0.1	54.7	9.0	18.3	5.2	3.2
090709630	268844864	93.59	64.08	0.1	46.9	30.0	7.0	7.0	2.4
090711850	269036608	139.61	−64.74	1.0	12.7	46.0	1.6	2.3	1.5
090712160	269063456	70.10	22.52	0.0	33.4	150.0	1.6	5.3	1.6
090713020	269137760	284.80	−3.33	2.4	59.0	51.0	4.7	8.0	4.2
090717111	269491232	246.95	22.97	3.9	35.1	1.0	84.6	5.2	1.4
090718720	269630208	243.76	−6.68	5.9	35.7	147.0	2.4	6.6	2.2
090720710	269802176	203.00	−54.80	2.9	56.0	8.0	40.5	9.7	4.6
090722447	269952224	344.13	−62.00	31.9	1.3	154.0	1.5	4.6	1.7
090726218	270278048	238.70	32.50	6.9	52.8	8.0	...	...	...
090807832	271367872	326.90	7.23	2.6	45.0	158.0	1.6	4.8	2.0
090811696	271701728	277.05	22.22	7.5	36.7	2.0	118.8	6.4	2.1
090813174	271829440	225.80	88.60	0.0	35.3	8.0	11.1	3.9	1.4
090814368	271932576	335.90	60.30	5.9	59.0	1.0	166.6	6.2	2.3
090815946	272068896	251.30	52.90	2.4	47.5	1.0	102.0	3.5	1.6
090819607	272385280	49.10	−67.10	3.3	47.0	1.0	103.9	5.9	2.4
090820509	272463200	321.00	−4.30	10.5	44.2	12.0	8.5	3.1	1.2
090826068	272943456	140.62	−0.11	9.7	27.1	8.0	11.6	2.8	1.1
090829672	273254848	329.20	−34.20	1.0	48.4	92.0	1.8	5.9	1.6
090829702	273257440	355.00	−9.40	3.2	42.0	24.0	5.3	5.5	2.1

Table 1
(Continued)

GRB Index	MET[a] (s)	R.A. (°)	Decl. (°)	Error (°)	Angle[b] (°)	T100 (s)	$F_{\rm lim,T100}$	$F_{\rm lim,30\,s}$	$F_{\rm lim,100\,s}$
							($\times 10^{-5}$ photons cm^{-2} s^{-1})		
090902462	273582304	264.94	27.32	0.0	50.8	30.0	265.2	265.3	84.6
090907808	274044224	81.10	20.50	3.7	32.0	1.0	...	3.1	0.9
090909854	274220992	54.18	−25.03	8.3	53.0	1.0	128.5	5.4	2.8
090917661	274895488	222.60	−19.80	7.4	37.9	3.0	40.7	3.8	1.6
090922539	275316992	13.10	74.00	1.0	20.0	146.0	1.2	3.4	1.3
090924625	275497184	50.80	−68.80	6.7	55.0	1.0	146.6	4.8	1.6
090926181	275631616	353.40	−66.32	0.0	48.1	30.0	274.7	274.8	99.9
091002685	276193568	41.00	−13.10	3.8	15.9	3.0	32.2	2.3	1.2
091003191	276237344	251.52	36.62	0.0	12.2	38.0	11.7	11.1	6.9
091010113	276835392	298.67	−22.54	0.1	55.7	15.0	18.7	9.1	3.2
091017985	277515552	204.80	−62.60	3.6	13.6	1.0	64.1	2.8	1.3
091019750	277668032	226.03	80.33	12.8	56.0	1.0	145.0	8.3	2.2
091020977	277773984	187.80	−13.40	2.2	44.9	38.0	7.4	9.5	4.2
091024380	278068000	339.25	56.89	0.0	15.5	36.0	2.0	2.5	1.0
091030613	278606592	249.00	23.54	5.6	47.9	148.0	1.8	4.5	2.6
091031500	278683232	71.70	−57.50	0.0	24.0	43.0	3.7	5.5	4.3
091103912	278978048	170.70	11.34	1.8	59.0	20.0	9.1	7.8	2.9
091107635	279299648	188.69	32.65	9.0	47.0	2.0	109.1	5.7	2.2
091109895	279494912	247.72	42.31	4.1	21.0	26.0	4.1	3.5	1.2
091115177	279951296	279.37	68.04	6.0	51.1	9.0	18.9	...	1.6
091120191	280384480	226.81	−21.79	0.5	46.0	53.0	4.2	6.9	2.4
091122163	280554848	91.28	6.02	17.7	56.0	1.0	146.0	6.8	3.4
091126389	280920000	48.72	28.26	12.6	57.0	1.0	167.7	11.1	2.6
091127976	281057152	36.60	−19.00	0.0	25.3	14.0	7.4	3.3	1.1
091202072	281411040	255.32	1.44	9.9	34.0	14.0	6.0	2.7	1.4
091207333	281865600	12.04	−48.42	1.7	36.3	146.0	1.1	3.1	1.2
091208410	281958592	29.40	16.90	0.0	55.6	16.0	25.3	17.8	4.7
091219462	282913472	294.49	71.91	5.4	36.0	1.0	78.6	3.4	0.8
091220442	282998208	167.76	3.92	1.5	60.1	23.0	12.3	9.0	2.1
091221870	283121568	55.80	23.20	0.0	53.4	34.0	5.8	6.6	1.5
091223191	283235712	203.23	76.35	8.9	33.0	1.0	77.6	2.7	1.0
091230260	283846464	101.53	0.68	18.0	59.0	1.0	149.9	5.2	1.7
091231206	283928192	197.09	−55.95	1.5	32.2	146.0	2.3	6.4	2.4
100101028	283999200	307.32	−27.00	17.4	31.0	1.0	85.8	4.4	1.7
100101988	284082144	70.66	18.69	9.3	47.0	1.0	102.0	4.0	1.2
100107074	284521600	6.31	−21.24	6.0	53.0	111.0	1.6	5.9	1.4
100111176	284875968	247.00	15.60	0.0	32.2	8.0	11.5	3.3	0.9
100112418	284983264	242.16	−77.54	14.0	57.0	25.0	8.2	6.5	3.4
100116897	285370272	305.00	14.50	0.0	26.5	108.0	1.2	4.1	1.5
100122616	285864448	79.20	−2.71	1.3	49.2	29.0	3.9	3.8	1.1
100130729	286565376	21.19	−24.75	2.5	48.0	92.0	1.3	4.0	1.2
100131730	286651872	120.39	16.49	1.2	27.0	11.0	10.3	5.8	2.3
100201588	286725984	133.10	−37.29	4.3	45.1	147.0	1.2	4.4	1.6
100204024	286936448	50.78	−47.89	3.0	55.1	30.0	6.6	6.6	1.7
100206563	287155808	47.16	13.16	0.0	44.7	2.0	100.5	3.5	1.5
100207721	287255904	321.78	−15.78	1.0	15.0	1.0	167.9	6.6	1.8
100208386	287313344	260.25	27.53	29.3	55.0	1.0	147.8	8.1	2.3
100210101	287461504	244.38	16.08	6.1	64.0	6.0	57.0	13.7	3.4
100212550	287673120	134.27	32.22	1.4	8.0	4.0	20.5	2.7	1.3
100212588	287676448	1.82	45.96	5.0	21.6	3.0	33.3	2.3	0.8
100218194	288160736	206.64	−11.94	2.2	37.5	147.0	1.0	4.9	1.3
100221368	288435040	27.12	−17.41	8.0	60.0	12.0	...	...	...
100225115	288758720	310.30	−59.40	0.9	58.2	12.0	27.7	13.9	4.5
100225580	288798944	314.27	0.21	1.1	55.1	8.0	33.1	11.4	3.6
100225703	288809536	147.91	34.01	3.9	49.9	12.0	15.2	5.9	3.3
100227067	288927392	0.00	0.00	0.0	35.6	0.0	0.8	2.7	0.8
100228873	289083456	117.99	18.63	11.1	55.0	4.0	49.1	6.9	3.4
100301068	289100256	110.14	−15.68	7.3	42.9	1.0	125.8	3.4	1.4
100301223	289113696	201.85	19.83	4.9	56.0	9.0	18.4	7.9	2.3
100313288	290156064	172.71	−52.58	2.9	59.1	7.0	27.8	5.8	2.7
100313509	290175136	186.37	11.72	9.6	43.8	28.0	3.6	3.3	1.3
100315361	290335168	208.90	30.14	5.5	7.0	1.0	62.2	2.2	0.8
100325246	291189280	209.14	−79.10	7.2	12.1	7.0	21.4	4.1	1.4
100325275	291191776	330.24	−26.47	0.9	9.1	8.0	18.8	6.2	2.1
100327405	291375808	334.93	−5.83	14.2	20.0	20.0	3.5	2.3	0.7

Table 1
(Continued)

GRB Index	MET[a] (s)	R.A. (°)	Decl. (°)	Error (°)	Angle[b] (°)	T100 (s)	$F_{\rm lim,T100}$	$F_{\rm lim,30\,s}$	$F_{\rm lim,100\,s}$
							($\times 10^{-5}$ photons cm^{-2} s^{-1})		
100328141	291439360	155.94	47.03	4.8	58.0	1.0	166.2	15.2	4.4
100330856	291673984	326.38	−6.97	7.7	21.0	24.0	3.0	2.4	0.8
100401297	291798464	281.85	−27.83	9.0	27.0	82.0	1.5	4.0	1.4
100414097	292904416	192.11	8.69	0.0	60.7	147.0	18.6	65.3	20.2
100417166	293169600	261.31	50.38	9.2	15.0	1.0	65.4	2.3	0.9
100420008	293415136	120.55	−5.82	2.8	58.7	25.0	10.3	8.6	2.9
100423244	293694688	119.67	5.78	1.5	40.3	13.0	7.6	6.0	2.0
100424876	293835712	7.79	43.35	2.4	53.5	27.0	7.0	6.3	1.7
100427356	294049920	89.17	−3.46	0.4	28.6	11.0	7.0	4.8	1.9
100429999	294278400	89.09	−69.96	4.0	41.0	9.0	10.6	2.9	...
100503554	294585472	147.48	3.96	1.5	61.6	135.0	2.4	8.0	3.2
100507577	294933088	2.90	−79.01	2.5	64.0	25.0	21.2	23.3	11.3
100511035	295231808	109.29	−4.65	1.0	43.6	41.0	2.6	3.6	1.1
100516014	295662016	117.32	55.14	5.3	19.0	1.0	66.7	2.5	1.1
100517132	295758592	40.63	−44.32	5.2	25.0	12.0	6.2	2.3	0.9
100519204	295937600	191.49	57.41	1.0	60.3	85.0	4.5	12.3	3.7
100527795	296679872	226.83	19.78	1.9	53.9	50.0	2.8	4.6	3.0
100528075	296704096	311.12	27.81	0.1	49.7	149.0	0.9	3.9	1.3
100604287	297327232	248.30	−73.19	3.6	52.0	13.0	13.4	5.6	1.9
100605774	297455712	273.43	−67.60	7.7	18.0	1.0	66.9	2.4	0.9
100608382	297681024	30.54	20.45	5.3	39.0	5.0	20.3	3.7	1.5
100614498	298209440	224.76	40.87	3.0	53.1	1.0	131.8	4.6	1.8
100620119	298695104	80.10	−51.68	1.5	20.1	21.0	7.0	4.8	1.5
100621529	298816928	160.86	14.72	11.4	64.0	1.0	286.7	10.7	3.0
100625891	299193760	338.26	20.29	4.4	30.8	9.0	8.8	2.5	1.0
100704149	299907296	133.64	−24.22	0.0	63.2	19.0	12.9	10.0	3.7
100715477	300886048	299.27	−54.71	9.3	42.0	14.0	7.0	3.1	1.6
100717446	301056096	304.31	19.53	9.2	59.0	1.0	165.7	9.9	2.4
100718160	301117824	121.83	−46.18	5.9	49.8	121.0	2.6	4.5	2.3
100719311	301217312	304.87	−67.14	15.4	43.0	1.0	96.0	3.7	1.5
100719825	301261696	231.41	18.56	10.3	58.0	1.0	167.4	6.5	1.6
100722096	301457920	238.77	−15.61	1.1	32.9	13.0	6.6	2.8	1.0
100724029	301624928	124.16	74.42	1.0	51.3	100.0	6.6	11.1	6.6
100725475	301749888	292.26	76.20	4.0	19.2	1.0	66.6	2.6	1.3
100728095	301976256	88.76	−15.26	0.0	59.9	147.0	6.4	19.8	7.2
100728439	302005920	44.05	0.28	0.1	57.0	6.0	33.6	5.8	1.8
100729415	302090240	349.59	−74.86	102.8	5.6	23.0	...	...	...
100802240	302420736	2.47	47.75	0.0	64.8	150.0	8.0	16.7	14.2
100805845	302732192	112.72	−35.93	3.8	64.7	44.0	8.9	15.8	3.8
100811108	303186944	345.87	15.86	6.0	64.0	1.0	229.4	26.4	10.1
100811781	303245056	108.14	62.19	3.6	17.9	16.0	5.7	2.9	1.2
100820373	303987424	258.79	−18.51	2.1	50.0	2.0	120.9	4.8	2.2
100826957	304556320	286.43	−32.63	3.8	64.2	103.0	4.0	9.9	3.8
100829374	304765152	115.45	−3.99	4.7	61.3	80.0	3.9	7.4	3.2
100905907	305416000	262.65	13.08	4.0	61.9	12.0	32.9	12.4	4.8
100910818	305840256	238.10	−34.62	1.0	50.8	21.0	8.2	7.8	4.7
100911816	305926528	151.32	58.99	11.8	59.0	1.0	12910.0	9.4	3.4
100919884	306623552	163.24	6.02	1.8	42.1	14.0	6.9	3.3	1.4
100923844	306965728	106.12	39.60	5.3	34.0	16.0	5.6	41.1	2.2
100924165	306993504	0.67	7.00	0.0	51.0	33.0	...	...	...
100926694	307212000	43.58	−11.10	12.0	46.0	1.0	113.3	6.1	2.4
100929235	307431520	166.33	62.29	13.4	41.0	1.0	85.2	2.9	1.0
101013412	308656352	292.08	−49.64	1.6	40.0	148.0	1.9	4.4	1.6
101014175	308722304	26.94	−51.07	1.0	54.1	116.0	2.8	6.6	...
101015558	308841856	73.16	15.46	5.9	57.0	21.0	13.5	9.5	...
101017619	309019904	27.47	−26.55	4.9	35.9	20.0	4.1	3.1	1.0
101025146	309670208	240.19	−8.49	24.4	55.0	1.0	134.6	7.0	2.2
101027230	309850240	79.02	43.97	11.4	30.0	1.0	75.1	3.8	1.0
101101899	310340064	266.04	−29.00	5.4	60.2	17.0	19.2	10.1	6.7
101102840	310421408	284.68	−37.03	7.8	39.1	148.0	1.0	2.9	1.2
101107011	310781792	168.33	22.43	4.1	36.2	147.0	1.4	2.7	1.1
101112984	311297824	100.10	9.62	5.1	46.9	70.0	1.8	4.2	1.2
101113483	311340928	29.08	0.21	2.7	46.3	147.0	0.9	3.6	1.1
101116481	311599936	32.00	−81.20	7.3	13.0	1.0	66.5	3.1	1.2
101126198	312439456	84.77	−22.55	1.0	63.5	25.0	10.5	8.9	2.9

Table 1
(Continued)

GRB Index	MET[a] (s)	R.A. (°)	Decl. (°)	Error (°)	Angle[b] (°)	T100 (s)	$F_{\rm lim,T100}$	$F_{\rm lim,30\,s}$	$F_{\rm lim,100\,s}$
							($\times 10^{-5}$ photons cm^{-2} s^{-1})		
101127093	312516832	290.31	7.89	23.2	64.9	1.0	282.1	12.4	7.6
101127102	312517664	70.95	−11.32	6.6	29.4	14.0	5.6	2.6	0.8
101128322	312623040	145.47	−35.20	5.7	7.0	2.0	62.1	3.1	0.8
101129652	312737984	157.75	−17.25	4.6	26.0	1.0	69.8	3.8	1.6
101129726	312744320	271.54	1.01	8.2	41.0	1.0	85.6	5.9	1.3
101204343	313143264	191.91	55.67	10.4	44.0	43.0	3.6	5.0	2.7
101206036	313289536	164.08	−38.11	3.5	57.5	8.0	25.2	12.8	3.2
101207536	313419104	175.75	8.72	3.7	57.3	148.0	1.3	6.2	1.6
101208203	313476768	212.40	4.04	11.7	39.2	1.0	...	...	...
101213849	313964544	260.99	−64.51	7.1	51.0	147.0	1.2	4.3	1.8
101214993	314063392	185.97	−24.27	10.0	60.0	13.0	16.2	6.7	2.1
101219686	314468896	12.23	−34.57	0.0	53.2	12.0	17.6	8.7	4.2
101220576	314545792	241.57	46.14	1.2	14.7	85.0	1.0	2.5	0.8
101220864	314570624	2.70	27.20	1.5	63.5	33.0	8.3	9.0	3.0
101224578	314891584	289.14	−55.25	4.8	49.6	47.0	2.9	3.7	1.3
101227406	315135904	240.50	−24.50	1.6	5.0	10.0	7.2	2.2	0.9
101227536	315147104	150.87	−49.44	2.6	57.7	16.0	11.5	8.3	4.0

Notes.
[a] Mission elapsed time relative to 2001 January 1, 0h:0m:0s UTC.
[b] Off-axis angle with respect to the LAT boresight.

We defined a subsample of 92 bursts that had a rate trigger greater than 75 counts s^{-1} in at least 1 of the 2 BGO detectors. This criteria is similar to the one adopted by Bissaldi et al. (2011) in their analysis of the brightest GBM-detected bursts in the first year of observations. Hereafter, we refer to these 92 bursts as the "bright BGO subsample;" it comprises likely candidates for which it would be possible to find evidence of spectral curvature above the upper boundary of the nominal BGO energy window of ∼40 MeV. Finally, we define our so-called spectroscopic subsample as the 30 bursts (of the bright BGO subsample) that have sufficient counts at higher energies to allow for the β index of a Band function fit to be determined with standard errors $\leqslant$0.5. This spectroscopic subsample was used in joint fits with the LAT data to test models containing spectral breaks or cutoffs.

4. ANALYSIS

4.1. LAT Upper Limits

We derive upper limits for the 288 GRBs that were detected by the GBM and fell in the LAT FOV from the LAT data using two methods. The first consists of the standard unbinned likelihood analysis using the software developed and provided by the LAT team, while the second method simply considers the total observed counts within an energy-dependent acceptance cone centered on the GBM burst location. The likelihood analysis will give more constraining upper limits, but since it uses the instrumental point-spread-function (PSF) information to model the spatial distribution of the observed photons, in cases where the burst location is inaccurate and burst photons are present, it can give less reliable constraints. The latter method will be less constraining in general, but it will also be less sensitive to errors in the burst location, as the analysis considers photons collected over a fixed aperture and does not otherwise use the burst or photon positions on the sky. We use both methods to obtain photon flux upper limits over a 0.1–10 GeV energy range.

For the unbinned likelihood analysis, we used the standard software package provided by the LAT team (ScienceTools version v9r15p6).[56] We selected "transient" class events in a 10° acceptance cone centered on the burst location, and we fit the data using the `pyLikelihood` module and the `P6_V3_TRANSIENT` response functions (Atwood et al. 2009). Each burst is modeled as a point source at the best available location, derived either from an instrument with good localization capabilities (e.g., *Swift* or LAT) or by the GBM alone. Of the 288 GRBs considered here, in the likelihood fitting, the expected distribution of counts is modeled using the energy-dependent LAT PSF and a power-law source spectrum. The photon index of the power law is fixed to either the β value found from the fit of the GBM data for that burst or, if the GBM data are not sufficiently constraining (i.e., $\delta\beta \leqslant 0.5$), to $\beta = -2.2$, the mean value found for the population of BATSE-detected bursts (Preece et al. 2000; Kaneko et al. 2006). An isotropic background component is included in the model, and the spectral properties of this component are derived using an empirical background model (Abdo et al. 2009c) that is a function of the position of the source in the sky and the position and orientation of the spacecraft in orbit. This background model accounts for contributions from both residual charged particle backgrounds and the time-averaged celestial gamma-ray emission.

Since we are considering cases where the burst flux in the LAT band will be weak or zero, the maximum likelihood estimate of the source flux may actually be negative owing to downward statistical fluctuations in the background counts. Because the unbinned likelihood function is based on Poisson probabilities, a prior assumption is imposed that requires the source flux to be non-negative. This is necessary to avoid negative probability densities that may arise for measured counts that are found very close to the GRB point-source location because of the sharpness of the PSF. On average, this means that for half of the cases in the null hypothesis (i.e., zero burst flux), the "best-fit" value of the source flux is zero but does not correspond to a local maximum of the unconstrained likelihood function (Mattox et al. 1996).

Given the prior of the non-negative source flux, we treat the resulting likelihood function as the posterior distribution of the

[56] http://fermi.gsfc.nasa.gov/ssc/

flux parameter. In this case, an upper limit may be obtained by finding the flux value at which the integral of the normalized likelihood corresponds to the chosen confidence level (Amsler et al. 2008). For a fully Bayesian treatment, one would integrate over the full posterior distribution, i.e., marginalize over the other free parameters in the model. However, in practice, we have found it sufficient to treat the profile likelihood function as a one-dimensional probability distribution function in the flux parameter. Again, in the limit of Gaussian statistics and a strong source, this method is equivalent to the use of the asymptotic standard error for defining confidence intervals. Hereafter, we will refer to this treatment as the "unbinned likelihood" method.

In the second set of upper limit calculations, we implement the method described by Helene (1983) and the interval calculation implemented in Kraft et al. (1991). Here, the upper limit is computed in terms of the number of counts and is based on the observed and estimated background counts within a prescribed extraction region. For the LAT data, the extraction region is an energy-dependent acceptance cone centered on the burst position. Since the burst locations from the GBM data have typical systematic uncertainties $\sim 3.^{\circ}2$ (Connaughton et al. 2011), the size of the acceptance cone at a given energy is taken to be the sum in quadrature of the LAT 95% PSF containment angle and the total (statistical + systematic) uncertainty in the burst location. The counts upper limits are evaluated over a number of energy bands, converted to fluxes using the energy-dependent LAT exposure at the burst location, and then summed to obtain the final flux limit. Since this method relies on comparing counts without fitting any spectral shape parameters, we will refer to this as the "counting" method.

The time intervals over which the upper limits are calculated are important for their interpretation. For both upper limit methods, we consider three time intervals: two fixed intervals of 30 and 100 s post-trigger, and a "T100" interval that is determined through the use of the Bayesian Blocks algorithm (Jackson et al. 2005) to estimate the duration of burst activity in the NaI detector that has the largest signal above background. For the T100 interval, an estimate of the time-varying background count rate is obtained by fitting a third-degree polynomial to the binned data in time intervals outside of the prompt burst phase. Nominally, we take $T_0 - dt$ to $T_0 - 100$ s and $T_0 + 150$ s to $T_0 + dt$, where T_0 is the GBM trigger time and $dt = 200$ s, although we increased the separation of these intervals in some cases to accommodate longer bursts. The counts per bin is then subtracted by the resulting background model throughout the $T_0 - dt$ to $T_0 + dt$ interval, and the binned reconstruction mode of the Bayesian Blocks algorithm is applied. The T100 interval is then defined by the first and last change points in the Bayesian Blocks reconstruction.

The two fixed time intervals have been introduced so as to not bias our results through assumptions regarding the durations of the high-energy components. The brighter LAT-detected GRBs have exhibited both delayed and extended high-energy emission on timescales that exceed the durations traditionally defined by observations in the keV–MeV energy range (Abdo et al. 2011). Hence, we search for and place limits on emission over intervals that may, in some cases, exceed the burst duration. We will discuss the implications of the limits found for the various time intervals in Section 5.1.

4.2. GBM Spectroscopy

For the 92 bursts in the bright BGO subsample, we performed spectral fits to the NaI and BGO data and estimated the flux expected to be seen by the LAT between 0.1–10 GeV using the GBM-fitted Band function (Band et al. 1993) parameters. The selection of background and source intervals for all bursts were performed manually through the use of the RMFIT (version 3.3) spectral analysis software package.[57] Because the number of counts in the highest BGO energy bins is often in the Poisson regime, we use the Castor modification (J. Castor 1995, private communication) to the Cash statistic (Cash 1976), commonly referred to as C-Stat,[58] since the standard χ^2 statistic is not reliable for low counts. The variable GBM background for each burst is determined for all detectors individually by fitting an energy-dependent, second-order polynomial to the data several hundred seconds before and after the prompt GRB emission. The standard 128 energy bin CSPEC data (Meegan et al. 2009) from the triggered NaI and BGO detectors were then fit from 8 keV to 1 MeV and from 200 keV to 40 MeV, respectively, for each burst.

As we noted above, only 30 bursts in the bright BGO subsample have sufficient signal to noise to constrain the high-energy power-law index β of the Band function to within ± 0.5. Although we considered a variety of models in our spectral analysis, we found that the Band function was sufficient to describe the spectral shape for all of these bursts.

5. RESULTS

5.1. LAT Upper Limits

Of the 288 GRBs in our sample, we were able to obtain upper limits, at 95% confidence level (CL), for 270 bursts using the unbinned likelihood method and 95% CL upper limits for 250 bursts using the counting method for the T100 intervals derived from the GBM data. The GRBs for which upper limits could not be calculated were bursts that occurred either during spacecraft passages through the South Atlantic Anomaly or at angles with respect to Earth's zenith that were $\gtrsim 100^{\circ}$, thereby resulting in diffuse emission at the burst locations that was dominated by γ-rays from Earth's limb produced by interactions of cosmic rays with Earth's atmosphere. These cases where the burst occurred at a high angle with respect to the zenith primarily affect the counting method, because it requires a reliable estimate of the background during the burst, and our method to estimate the background does not account for Earth limb emission. The likelihood method can fit for an Earth limb as a diffuse component, but it may give weaker limits since the background level is not as tightly constrained in this case compared to when the empirical background estimate can be used to model all of the non-burst emission. The photon flux upper limits found for the likelihood method for all three time intervals are presented in the last three columns of Table 1.

The distributions of the 95% CL photon flux upper limits obtained via the likelihood and counting methods for the 30 s, 100 s, and T100 time intervals are shown in upper-left, upper-right, and lower-left panels of Figure 2, respectively. As expected, the likelihood limits are systematically deeper than those found using the counting method over the same time interval. For either method, the upper limits for the 100 s integrations are roughly half an order of magnitude deeper than for the 30 s integrations. In the photon-limited case, this is expected since the flux limit at a specified confidence level should be inversely proportional to the exposure. The doubly peaked upper limit

[57] http://fermi.gsfc.nasa.gov/ssc/data/analysis/user/
[58] http://heasarc.nasa.gov/xanadu/xspec/manual/manual.html

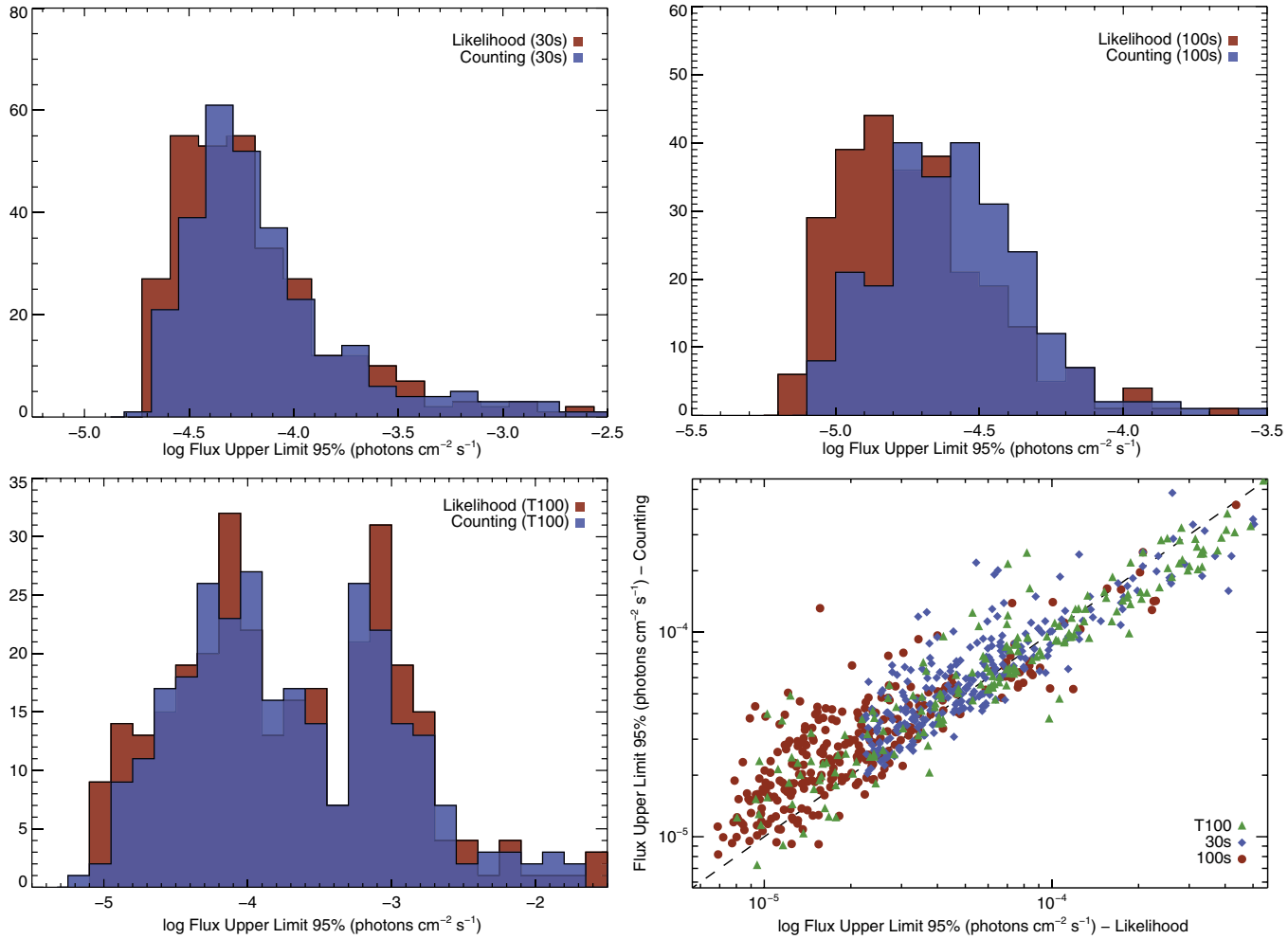

Figure 2. Distributions of the 95% CL photon flux upper limits obtained via the likelihood and counting methods for the 30 s (upper-left), 100 s (upper-right), and T100 (lower-left) time intervals. A scatter plot comparison of the upper limits calculated over the three intervals is shown in the lower-right panel. The dashed line represents the line of equality between the likelihood and counting methods.

(A color version of this figure is available in the online journal.)

distribution that appears in the upper-left panel of Figure 2 for the T100 duration reflects the bimodal duration distribution for the short and long GRB populations. The median of the T100 upper limit distribution for the likelihood method is $\tilde{F}_{\rm UL,T100} = 1.20\times10^{-4}$ photons cm^{-2} s^{-1} with a standard deviation of $\sigma_{T100} = 1.57\times10^{-3}$; whereas the counting method distribution has a median of $\tilde{F}_{\rm UL,T100} = 1.27\times10^{-4}$ photons cm^{-2} s^{-1} and $\sigma_{T100} = 1.52 \times 10^{-3}$. The median of the 30 s upper limit distribution for the likelihood method is $\tilde{F}_{\rm UL,30s} = 4.76 \times 10^{-5}$ photons cm^{-2} s^{-1} with a standard deviation of $\sigma_{30s} = 3.20 \times 10^{-4}$; whereas the counting method distribution has a median of $\tilde{F}_{\rm UL,30s} = 5.46 \times 10^{-5}$ photons cm^{-2} s^{-1} and $\sigma_{30s} = 3.00 \times 10^{-4}$. The median of the 100 s upper limit distribution for the likelihood method are $\tilde{F}_{\rm UL,100s} = 1.74 \times 10^{-5}$ photons cm^{-2} s^{-1} and $\sigma_{100s} = 1.23\times10^{-4}$ and $\tilde{F}_{\rm UL,100s} = 2.59 \times 10^{-5}$ photons cm^{-2} s^{-1} and $\sigma_{100s} = 1.06 \times 10^{-4}$ for the counting method.

A comparison of the likelihood and counting methods for all three time intervals for is shown in the lower-right panel of Figure 2. The scatter in the upper limit distribution for both methods is largely due to the range of angles at which the GRBs occurred with respect to the LAT boresight, resulting in different effective areas and hence different exposures for each burst. The LAT exposure as a function of the off-axis angle drops steeply with increasing inclination, resulting in a shallowing of the LAT upper limits as a function of increasing off-axis angle, which can be seen in Figure 3. Overall, the two methods give consistent results for the bursts in our sample, and therefore we will hereafter focus primarily on the limits obtained with the likelihood method in our discussion of the implication of these results.

Despite the dependence of the upper limit values on off-axis angle, the distribution of LAT photon flux upper limits is relatively narrow for angles $< 40^\circ$, allowing us to define an effective LAT sensitivity assuming a typical GRB spectrum (i.e., $\beta \approx -2.2$). We can therefore set sensitivity thresholds for the corresponding median photon flux upper limit for each integration time of $F_{\rm lim,30\,s} = 4.7 \times 10^{-5}$ photons cm^{-2} s^{-1} and $F_{\rm lim,100\,s} = 1.6 \times 10^{-5}$ photons cm^{-2} s^{-1}.

Finally, in Figure 4 we plot the location of each burst on the sky in Galactic coordinates, color-coded to represent the likelihood-determined photon flux upper limits. There is no evidence of a spatial dependence of the GBM detection rate nor of the magnitude of the LAT upper limit, as a function of Galactic latitude b.

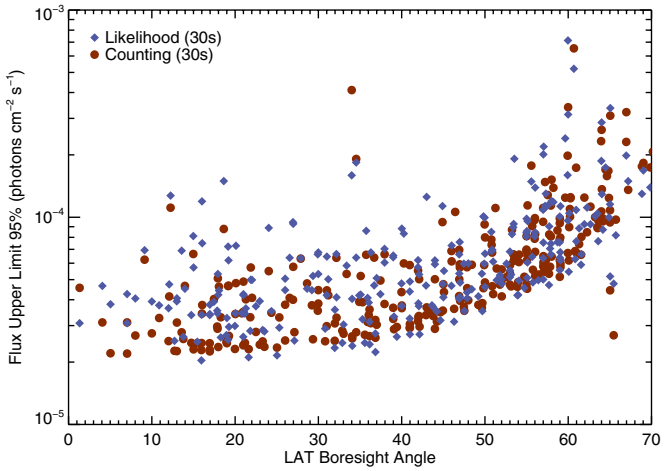

Figure 3. The 95% CL photon flux upper limits determined using the likelihood and counting methods as a function of off-axis angle. The decreasing exposure as a function of off-axis angle results in the shallowing of the LAT upper limits for bursts occurring away from the LAT boresight.

(A color version of this figure is available in the online journal.)

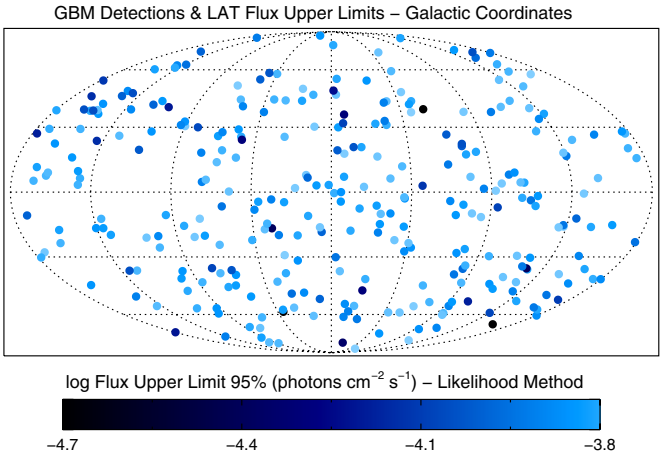

Figure 4. Celestial distribution of 288 gamma-ray bursts as detected by *Fermi*-GBM in the first 2.5 years of LAT operations that fell in the LAT FOV, plotted in Galactic coordinates. The colors represents the 95% CL LAT photon flux upper limits.

(A color version of this figure is available in the online journal.)

5.2. GBM Spectral Fits and Upper Limit Comparisons

We compare the LAT upper limits calculated over the burst duration to the expected 0.1–10 GeV photon fluxes found through extrapolations of spectral fits presented in the first GBM spectral catalog (Goldstein et al. 2012). We focus this analysis on bursts for which a Band spectral model was a preferred fit compared to models with fewer degrees of freedom, since alternative models such as Comptonized spectra suffer sharp drops in expected flux at high energy and are not expected to result in LAT detections without the presence of additional spectral components. Of the 487 GRBs presented in that catalog, a Band model fit was preferred over simpler models for 161 bursts, 75 of which appeared in the LAT FOV. For this comparison, the LAT upper limits were recalculated for a duration that matched the interval used in the GBM spectral catalog (see Goldstein et al. 2012 for a detailed discussion of their interval selection). We next performed a simulation in which we varied the expected LAT photon flux fitted values using the associated errors for each burst in order to determine

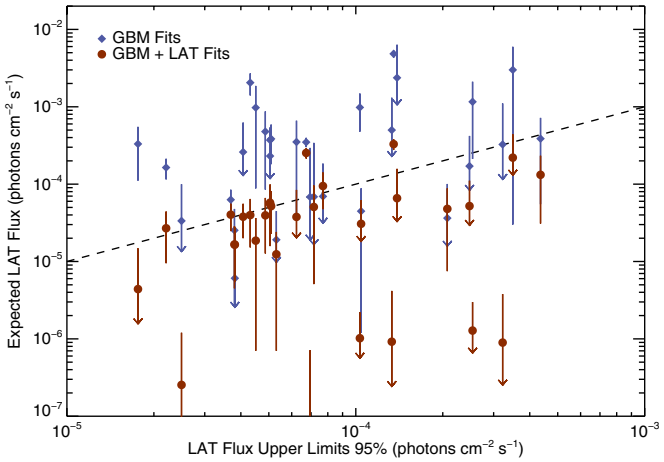

Figure 5. Expected photon flux, based on fits to the prompt GBM spectrum and duration plotted vs. the LAT flux upper limit for each burst. When fitting only to the GBM data, roughly 50% of the bursts in the spectroscopic sample have expected LAT fluxes that exceed the LAT 95% CL flux upper limit. When fitting both the GBM and LAT data, only 23% of our sample have expected flux values that exceed the 95% CL LAT flux upper limit. The dashed line represents the line of equality.

(A color version of this figure is available in the online journal.)

the median number of bursts over all realizations that would fall above the LAT upper limit. In a total of 10^5 realizations, we find that 50% of the GRBs in the GBM spectral catalog, which prefer a Band model fit, have expected 0.1–10 GeV photon fluxes that exceeds the LAT upper limit.

We investigate the differences between the GBM-based extrapolations and the LAT upper limits further by performing detailed spectral fits to our spectroscopic subsample. The spectral parameters obtained from the fits to the GBM data only for the 30 GRBs in this spectroscopic subsample are listed in Table 2. The median values of the low- and high-energy power-law indices and the peak of the νF_ν spectra are $\alpha = -0.83$, $\beta = -2.26$, and $E_{\rm pk} = 164$ keV, with standard deviations of $\sigma_\alpha = 0.44$, $\sigma_\beta = 0.25$, and $\sigma_{E_{\rm pk}} = 177$ keV, respectively. The distributions of spectral parameters for these bursts are consistent with similar distributions found for BATSE-detected GRBs (Preece et al. 2000; Kaneko et al. 2006). The time durations used in the spectral fits and the time-averaged photon flux values in the 0.02–20 MeV energy range for these GRBs are given in Table 3. In the third column, we list the expected flux in the 0.1–10 GeV energy range assuming a power-law extrapolation of the Band function fit to the GBM data; and in the fourth column, we give the measured LAT photon flux upper limit found for the same time interval. The errors on the expected LAT photon fluxes were determined using the covariance matrices obtained from the GBM spectral fits.

A comparison of the LAT photon flux upper limits versus the expected 0.1–10 GeV photon fluxes for each burst in our spectroscopic subsample is shown as blue data points in Figure 5. The downward arrows on the expected flux values indicate values that are consistent with zero within the 1σ errors shown. The dashed line represents the line of equality between the expected LAT photon flux and the LAT photon flux upper limits when calculated for the durations presented in Figure 5. In a total of 10^5 realizations, we find that 53% of GRBs in our spectroscopic subsample have expected 0.1–10 GeV photon fluxes that exceed their associated 95% CL LAT upper limit. As with the flux comparison, roughly 50% in our sample also have expected fluence values that exceed the 95% CL LAT

Table 2
Spectral Parameters for 30 Bright GBM-detected Bursts—GBM Fits

GRB	Amplitude ($\times 10^{-2}$ photons cm^{-2} s^{-1})	α	β	$E_{\rm pk}$ (keV)	C-Stat
080824909	0.65 ± 0.33	-1.02 ± 0.25	-1.84 ± 0.12	113.2 ± 47.6	1.27
080906212	12.07 ± 1.58	-0.42 ± 0.09	-2.38 ± 0.13	163.9 ± 11.8	1.29
080925775	1.87 ± 0.19	-1.00 ± 0.05	-2.13 ± 0.08	136.3 ± 11.6	1.32
081122520	4.19 ± 0.44	-0.64 ± 0.07	-2.44 ± 0.23	221.2 ± 19.9	1.02
081207680	0.97 ± 0.04	-0.66 ± 0.03	-1.98 ± 0.05	417.0 ± 24.8	2.44
081223419	4.84 ± 4.20	-0.25 ± 0.46	-1.85 ± 0.14	104.4 ± 33.3	1.03
081231140	1.50 ± 0.08	-1.07 ± 0.04	-2.59 ± 0.34	251.9 ± 20.6	1.38
090129880	0.65 ± 0.10	-1.52 ± 0.09	-2.31 ± 0.53	184.7 ± 62.5	1.10
090131090	2.70 ± 0.52	-1.11 ± 0.08	-2.17 ± 0.04	55.0 ± 4.2	1.85
090514006	1.54 ± 0.56	-0.81 ± 0.19	-2.10 ± 0.19	103.9 ± 21.4	1.12
090528516	2.38 ± 0.14	-1.00 ± 0.03	-2.19 ± 0.06	163.5 ± 8.9	2.43
090612619	1.24 ± 0.15	-0.81 ± 0.10	-2.30 ± 0.41	399.1 ± 80.6	1.18
090620400	1.81 ± 0.21	-0.45 ± 0.07	-2.53 ± 0.21	157.7 ± 9.8	1.26
090829672	1.88 ± 0.04	-1.59 ± 0.01	-2.27 ± 0.11	254.4 ± 20.1	2.62
091031500	0.72 ± 0.04	-0.91 ± 0.05	-2.28 ± 0.25	474.6 ± 58.5	1.54
091109895	50.12 ± 176.00	0.78 ± 1.57	-2.28 ± 0.23	46.3 ± 13.6	1.10
091120191	2.58 ± 0.27	-1.02 ± 0.06	-2.50 ± 0.13	101.4 ± 5.8	2.30
091127976	10.01 ± 1.61	-1.28 ± 0.06	-2.22 ± 0.02	34.1 ± 1.4	1.53
091208410	1.32 ± 0.20	-1.34 ± 0.08	-2.32 ± 0.24	110.3 ± 17.3	1.30
091221870	1.20 ± 0.17	-0.76 ± 0.10	-2.09 ± 0.12	205.7 ± 26.8	1.53
100122616	6.89 ± 1.65	-0.91 ± 0.10	-2.32 ± 0.04	42.7 ± 2.3	1.49
100131730	11.80 ± 1.32	-0.57 ± 0.06	-2.21 ± 0.08	138.1 ± 8.4	1.02
100225115	0.56 ± 0.06	-0.83 ± 0.09	-2.48 ± 0.74	493.4 ± 107.0	1.37
100225580	3.71 ± 0.46	-0.76 ± 0.08	-2.11 ± 0.12	194.5 ± 21.4	1.22
100724029	3.36 ± 0.04	-0.76 ± 0.01	-2.03 ± 0.02	413.1 ± 8.9	3.19
100728095	1.33 ± 0.02	-0.86 ± 0.02	-3.03 ± 0.35	413.5 ± 13.3	15.24
101126198	3.10 ± 0.13	-1.25 ± 0.02	-2.56 ± 0.15	156.7 ± 7.5	1.62
101206036	0.49 ± 0.11	-1.13 ± 0.16	-1.84 ± 0.28	467.6 ± 324.0	1.20
101227406	3.15 ± 0.91	-0.51 ± 0.19	-2.18 ± 0.13	148.9 ± 20.9	1.48
101227536	0.48 ± 0.03	-0.73 ± 0.08	-2.26 ± 0.32	828.2 ± 172.0	1.19

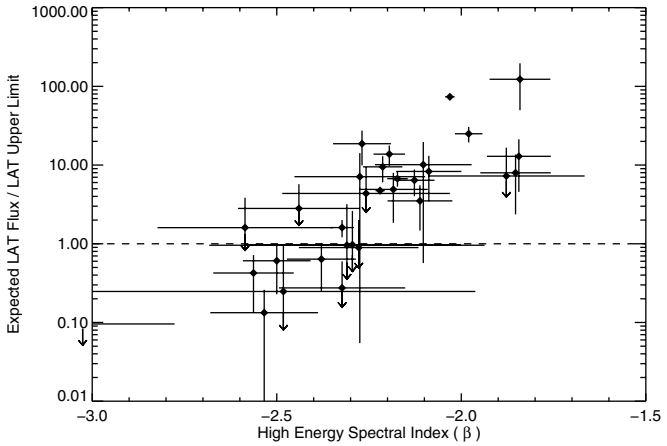

Figure 6. Ratio of the expected LAT flux, based on fits to the prompt GBM spectrum, to the LAT 95% CL LAT flux upper limit plotted vs. the GBM-determined high-energy spectral index. The degree to which the expected flux in the LAT energy range from these bursts exceeds our estimated LAT upper limits correlates strongly with the measured high-energy spectral index.

fluence upper limit. Figure 6 shows that the degree to which the expected flux in the LAT energy range from these bursts exceeds our estimated LAT upper limits correlates strongly with the measured high-energy spectral index, with particularly hard bursts exceeding the estimated LAT sensitivity by as much as a factor of 100. Again, the spectral fits to the bright bursts detected by the BGO clearly shows that a simple extrapolation from the GBM band to the LAT band systematically overpredicts the observed flux.

5.3. Joint GBM and LAT Spectral Fits

Including the LAT data in the spectral fits drastically alters the best-fit Band model parameters and the resulting expected photon flux in the LAT energy range. The best-fit parameters of the joint spectral fits for the spectroscopic subsample can be found in Table 4. The high-energy spectral indices are typically steeper (softer) than found from fits to the GBM data alone.

The difference in the β values for the joint fits with respect to the fits to the GBM data alone can be found in Column 8 of Table 4. The resulting β distributions are shown in Figure 7. The GBM-only β distribution (red histogram) peaks at $\beta = -2.2$, matching the β distribution found for the population of BATSE-detected bursts presented in Preece et al. (2000). In contrast, the β distribution found from the joint fits (blue histogram) indicates spectra that are considerably softer, with a median value of $\beta = -2.5$. While the GBM-only β distribution includes five GRBs with $\beta > -2.0$, no bursts had β values this hard from the joint fits. The low-energy power-law index α and the peak of the νF_ν spectra, $E_{\rm pk}$ distribution remain relatively unchanged. In Figure 5, we compare the LAT photon flux upper limits calculated over the burst duration presented in Table 4 versus the expected 0.1–10 GeV photon fluxes for each burst, now using a power-law extrapolation of the Band function that was fit to both the GBM and LAT data. The softer β values obtained through the joint fits yield expected LAT photon flux values that are more consistent with the LAT non-detections, with only 23% of the bursts in our spectroscopic subsample with expected flux values that exceed the 95% CL LAT flux upper limit given 10^5 realizations of the data about their errors. We find that a

Table 3
Measured and Expected Photon Fluxes in the GBM and LAT Bands

GRB	T90 (s)	Measured Flux 0.02–20 MeV (photons cm^{-2} s^{-1})	Expected Flux 0.1–10 GeV ($\times 10^{-4}$ photons cm^{-2} s^{-1})	Flux Limit 0.1–10 GeV ($\times 10^{-5}$ photons cm^{-2} s^{-1})
080824909	28.67	1.04 ± 0.04	9.75 ± 8.87	4.50
080906212	2.69	12.20 ± 0.18	3.87 ± 3.32	43.60
080925775	38.14	3.08 ± 0.03	3.85 ± 2.04	5.09
081122520	4.10	6.37 ± 0.12	1.71 ± 2.49	24.75
081207680	104.45	2.26 ± 0.02	20.50 ± 6.49	4.31
081223419	2.36	2.90 ± 0.13	30.00 ± 29.70	34.95
081231140	27.65	3.37 ± 0.04	0.34 ± 0.66	2.49
090129880	16.38	2.03 ± 0.05	0.68 ± 2.26	6.94
090131090	57.35	2.98 ± 0.03	1.64 ± 0.49	2.21
090514006	12.97	1.70 ± 0.06	2.31 ± 3.10	5.05
090528516	61.44	4.25 ± 0.03	3.71 ± 1.50	5.05
090612619	6.14	2.91 ± 0.09	3.26 ± 7.79	32.23
090620400	49.41	1.81 ± 0.03	0.19 ± 0.26	5.31
090829672	94.21	6.61 ± 0.03	3.31 ± 2.20	1.76
091031500	45.06	1.89 ± 0.03	2.60 ± 3.65	4.07
091109895	6.14	1.44 ± 0.11	0.36 ± 0.64	20.74
091120191	53.25	3.56 ± 0.04	0.25 ± 0.23	3.80
091127976	14.08	10.70 ± 0.05	3.49 ± 0.48	6.73
091208410	16.38	2.87 ± 0.06	0.69 ± 1.15	7.69
091221870	34.82	1.98 ± 0.04	4.78 ± 3.93	4.86
100122616	29.70	4.11 ± 0.04	0.63 ± 0.22	3.69
100131730	3.46	12.20 ± 0.15	9.81 ± 5.04	10.33
100225115	18.99	1.44 ± 0.05	0.69 ± 2.73	7.16
100225580	5.12	5.86 ± 0.10	11.60 ± 9.48	25.36
100724029	100.35	8.02 ± 0.03	48.40 ± 5.20	13.52
100728095	147.46	3.20 ± 0.02	0.06 ± 0.11	3.81
101126198	25.60	6.91 ± 0.05	0.45 ± 0.44	10.43
101206036	17.92	1.44 ± 0.07	23.70 ± 39.70	13.89
101227406	10.50	3.27 ± 0.10	3.51 ± 3.10	6.23
101227536	18.82	1.55 ± 0.05	5.00 ± 8.10	13.32

similar ratio of bursts have expected fluence values that exceed their associated 95% CL LAT fluence upper limit.

5.4. Spectral Breaks or Softer Spectral Indices?

Although the discrepancy between the predicted 0.1–10 GeV fluxes from the GBM-only fits and the LAT upper limits can be explained by the softer β values in the joint fits, intrinsic spectral breaks at energies $\gtrsim$ 40 MeV can also reconcile the conflicting GBM and LAT results. Determining whether softer β values or spectral breaks are present has at least two important implications: if the spectral breaks or cutoffs arise from intrinsic pair production ($\gamma\gamma \rightarrow e^+e^-$) in the source, then the break or cutoff energy would provide a direct estimate of the bulk Lorentz factor of the emitting region within the outflow. On the other hand, an intrinsically softer distribution of β values would mean that theoretical inferences based on the β distributions found by fitting BATSE or GBM data alone may need to be revised. Evidence for either spectral breaks or softer β values could also provide support for multi-component models that have been used to describe novel spectral features detected by the GBM and LAT (e.g., Guiriec et al. 2011).

For the joint fitting of the GBM and LAT data, deciding between the two possibilities for any single burst can be cast as a standard model selection problem. Under the null hypothesis, we model the GRB spectrum using a simple Band function, as we have done in Section 5.3. As an alternative hypothesis, we could extend the Band model to account for the presence of a spectral break. This may be done via an additional break energy above the Band $E_{\rm pk}$, effectively using a doubly broken power law

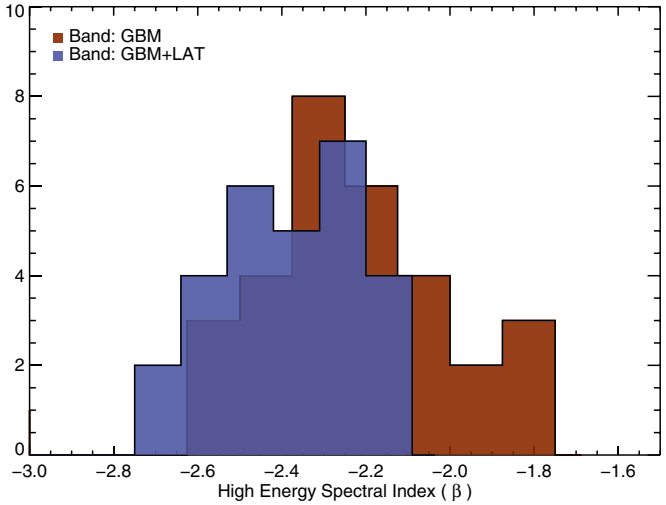

Figure 7. Comparison between the high-energy spectral indices measured through spectral fits to the GBM data alone and joint fits to both the GBM and LAT data. The GBM-only β distribution has a median value of $\beta = -2.2$, matching the distribution found by Preece et al. (2000) and Kaneko et al. (2006). In contrast, the β distribution found from the joint fits indicate spectra that are considerably softer, with a median value of $\beta = -2.5$.

(A color version of this figure is available in the online journal.)

in the fit; or it could be accomplished by adding an exponential cutoff to the Band model with cutoff energy $E_c > E_{\rm pk}$. In either case, the null and alternative hypotheses are "nested" such that the former is a special case of the latter for some values of the

Table 4
Spectral Parameters for 30 Bright GBM-detected Bursts—GBM and LAT Fits

GRB	Amplitude ($\times 10^{-2}$ photons cm^{-2} s^{-1})	α	β	$E_{\rm pk}$ (keV)	Cash	dof	$\Delta\beta$	ΔC-Stat
080824909	0.53 ± 0.12	-1.11 ± 0.13	-2.41 ± 0.15	151.2 ± 31.3	475.73	378	-0.56 ± 0.15	2.32
080906212	10.79 ± 1.10	-0.48 ± 0.07	-2.55 ± 0.12	176.4 ± 10.1	639.11	504	-0.17 ± 0.12	0.20
080925775	1.70 ± 0.12	-1.05 ± 0.04	-2.42 ± 0.09	154.0 ± 9.4	500.77	380	-0.30 ± 0.09	9.53
081122520	3.99 ± 0.35	-0.67 ± 0.07	-2.64 ± 0.19	232.7 ± 17.0	501.82	502	-0.20 ± 0.19	0.04
081207680	0.87 ± 0.02	-0.73 ± 0.02	-2.70 ± 0.12	528.2 ± 24.3	952.43	385	-0.72 ± 0.12	14.57
081223419	2.57 ± 1.02	-0.57 ± 0.25	-2.23 ± 0.15	149.6 ± 32.0	399.95	380	-0.37 ± 0.15	0.67
081231140	1.46 ± 0.07	-1.08 ± 0.03	-3.46 ± 0.71	265.7 ± 16.0	509.18	378	-0.88 ± 0.71	0.01
090129880	0.61 ± 0.07	-1.55 ± 0.07	-4.16 ± 36.00	219.9 ± 56.2	406.74	379	-1.85 ± 36.00	0.00
090131090	1.62 ± 0.16	-1.33 ± 0.05	-2.42 ± 0.09	73.8 ± 4.6	696.42	374	-0.25 ± 0.09	15.51
090514006	1.49 ± 0.41	-0.82 ± 0.15	-2.30 ± 0.10	109.1 ± 15.1	424.25	380	-0.19 ± 0.10	2.59
090528516	2.14 ± 0.09	-1.06 ± 0.03	-2.49 ± 0.11	187.2 ± 8.6	1216.40	504	-0.30 ± 0.11	9.20
090612619	1.18 ± 0.10	-0.84 ± 0.08	-3.41 ± 0.66	444.0 ± 65.5	436.14	379	-1.11 ± 0.66	0.00
090620400	1.77 ± 0.18	-0.47 ± 0.07	-2.60 ± 0.14	160.0 ± 8.6	469.50	377	-0.07 ± 0.14	0.08
090829672	1.83 ± 0.03	-1.60 ± 0.01	-3.07 ± 0.48	287.0 ± 17.3	972.98	379	-0.80 ± 0.48	0.39
091031500	0.70 ± 0.03	-0.92 ± 0.04	-2.63 ± 0.09	501.1 ± 50.2	567.74	378	-0.35 ± 0.09	0.02
091109895	54.26 ± 190.00	0.81 ± 1.58	-2.24 ± 0.11	45.6 ± 12.3	272.81	255	0.04 ± 0.11	-0.04
091120191	2.53 ± 0.24	-1.03 ± 0.05	-2.56 ± 0.11	103.1 ± 5.1	589.17	262	-0.06 ± 0.11	0.31
091127976	8.55 ± 1.16	-1.34 ± 0.06	-2.26 ± 0.02	36.4 ± 1.4	774.38	495	-0.04 ± 0.02	25.95
091208410	1.35 ± 0.20	-1.33 ± 0.07	-2.28 ± 0.07	107.4 ± 13.9	480.39	376	0.04 ± 0.07	0.07
091221870	1.06 ± 0.10	-0.84 ± 0.07	-2.48 ± 0.11	241.0 ± 22.8	571.15	379	-0.40 ± 0.11	2.67
100122616	6.01 ± 1.28	-0.96 ± 0.09	-2.38 ± 0.05	44.6 ± 2.3	557.59	379	-0.06 ± 0.05	5.13
100131730	8.07 ± 0.48	-0.78 ± 0.04	-3.32 ± 0.20	183.8 ± 7.3	399.27	382	-1.11 ± 0.20	2.59
100225115	0.56 ± 0.05	-0.83 ± 0.09	-2.54 ± 0.17	496.8 ± 94.8	506.20	379	-0.06 ± 0.17	-0.02
100225580	3.02 ± 0.21	-0.88 ± 0.05	-3.25 ± 0.24	248.8 ± 17.7	619.61	509	-1.14 ± 0.24	1.72
100724029	3.08 ± 0.03	-0.82 ± 0.01	-2.51 ± 0.03	502.1 ± 8.6	1435.30	378	-0.48 ± 0.03	170.70
100728095	1.33 ± 0.02	-0.86 ± 0.02	-2.84 ± 0.12	410.8 ± 12.4	5633.20	379	0.19 ± 0.12	0.70
101126198	3.08 ± 0.12	-1.26 ± 0.02	-2.62 ± 0.16	158.4 ± 7.2	603.71	379	-0.06 ± 0.16	0.37
101206036	0.49 ± 0.07	-1.12 ± 0.12	-2.45 ± 0.27	514.9 ± 209.0	445.33	378	-0.62 ± 0.27	0.06
101227406	2.18 ± 0.38	-0.74 ± 0.13	-2.53 ± 0.20	188.7 ± 21.3	549.62	378	-0.35 ± 0.20	3.26
101227536	0.47 ± 0.03	-0.75 ± 0.07	-3.65 ± 0.86	930.3 ± 164.0	440.63	378	-1.39 ± 0.86	0.01

extra model parameters that are introduced. Assuming there are $n_{\rm alt}$ additional free parameters under the alternative model, then whether the alternative model is statistically preferred would be given by the ΔC-Stat value assuming it follows a χ^2 distribution for $n_{\rm alt}$ degrees of freedom.

For the purposes of this analysis, we have adopted an alternative model consisting of a Band function plus a step function fixed at 50 MeV. The step function is not intended to be a physical model; instead its use is simply designed to test consistency between the GBM and LAT data. By using a step function we are explicitly avoiding making any assumptions as to the physical mechanism producing the emission, which allows us instead to focus on simply comparing the LAT upper limits to the extrapolation of the best fit to the GBM data. The additional degree of freedom introduced by the step function represents the normalization of the Band function's high-energy component above 50 MeV, which is left to vary, leading to the normalization of the power law above 50 MeV being adjusted such that it is always consistent with the LAT upper limits. For this analysis, the index of the power law above the break is fixed to match the Band function's high-energy power-law index, which is allowed to vary as a free parameter. Since this introduces a single extra degree of freedom, a value of ΔC-Stat >9 would represent a $>3\sigma$ improvement in the fit. We adopt this criterion as the threshold for a statistical preference for a break in the high-energy spectrum of an individual GRB.

An example of such a fit can be seen in Figure 8, where the three panels show (clockwise) a Band model fit to GBM data alone, a Band model fit to both the GBM and LAT data, and a Band model plus a step function fit to the GBM and LAT data. The difference between the first two panels demonstrates the degree to which the high-energy spectral index can steepen to accommodate the LAT data, despite being outside of the range allowed by the statistical uncertainty in the β determination made through the GBM fit alone. The third panel shows the effect of introducing a step function between the two instruments, in which the requirement for a softer β value is alleviated. For the fit shown in Figure 8, the β value determined through the Band model plus a step function fit is consistent with the value found by fitting a Band model to the GBM data alone.

The ΔC-Stat values obtained for the Band and Band+step function fits are listed in Column 9 of Table 4. For most of the bursts, a simple steepening of the high-energy power-law index was sufficient to explain the lack of a LAT detection. However, in six cases ΔC-Stat exceeded a value of 9, indicating a statistical preference for a break in the high-energy spectrum. Figure 9 shows the ratio of the expected LAT flux (based on GBM-only fits) to the LAT 95% CL upper limit plotted versus the ΔC-Stat values for the spectroscopic subsample. A weak correlation between the flux ratio and ΔC-Stat is apparent. In addition, Figure 10 shows an anti-correlation between the resulting ΔC-Stat values for this sample plotted versus the uncertainty in the high-energy spectral index found from fits to the GBM data alone. The bursts for which a spectral break is statistically preferred both have the most severe discrepancies between the GBM-only extrapolations and the LAT upper limits and also have the smallest uncertainties in their GBM-only β values.

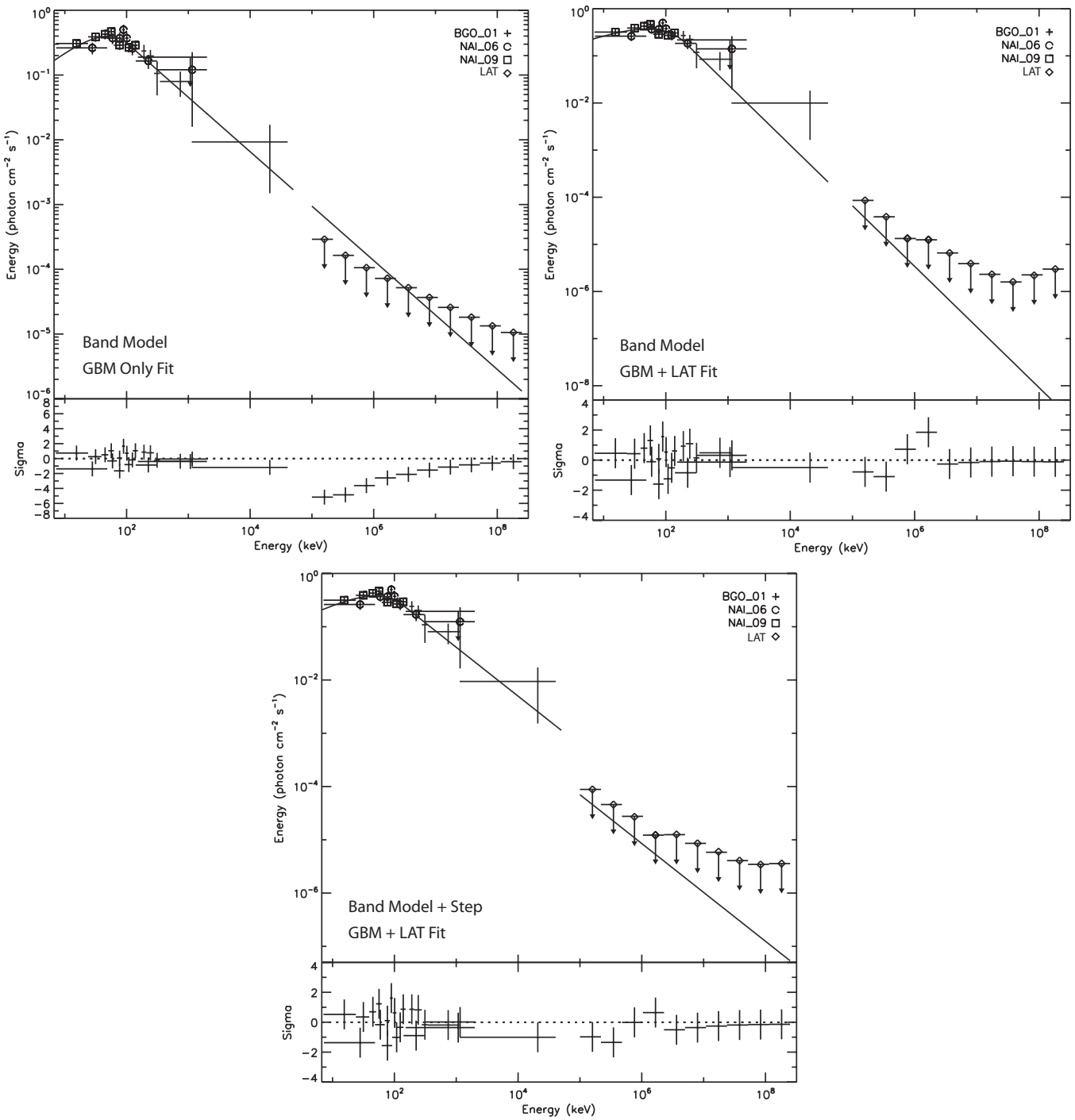

Figure 8. Example spectral fits showing (clockwise) a Band model fit to GBM data alone, a Band model fit to both the GBM and LAT data, and a Band model plus a step function fit to the GBM and LAT data.

5.5. Constraints on the Bulk Lorentz Factor

If we assume that the high-energy spectra in the six GRBs that prefer spectral cutoffs are a result of $\gamma\gamma$ attenuation, as opposed to a spectral turnover that is intrinsic to the GRB spectrum, then we can use the joint GBM and LAT spectral fits in conjunction with the LAT non-detections at 100 MeV to place limits on the maximum Lorentz factor. In this context, the high-energy γ-rays produced within the GRB jet may undergo $\gamma\gamma \rightarrow e^+e^-$ pair production and can be absorbed in situ. The interaction rate of this process and corresponding optical depth, $\tau_{\gamma\gamma}$, depend on the target photon density and can be significant when both the high-energy and target photons are produced in the same physical region. Highly relativistic bulk motion of such an emission region can reduce the implied $\gamma\gamma$ optical depth greatly by allowing for a larger emitting region radius and a smaller target photon density for a given observed flux and variability timescale. Observation of γ-ray emission up to an energy $E_{\rm max} \gg m_e c^2$ thus can be used to put a lower limit on the bulk Lorentz factor Γ of the emitting region (Lithwick & Sari 2001; Razzaque et al. 2004; Granot et al. 2008; Ackermann et al. 2010). This method is valid for $\Gamma \leqslant E_{\rm max}(1+z)/m_e c^2$, which

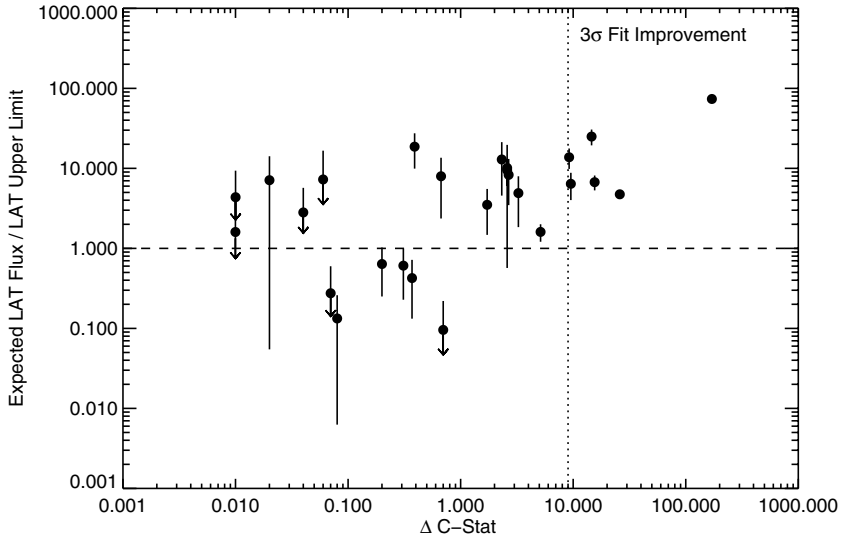

Figure 9. Ratio of the expected LAT flux (based on GBM-only fits) to the LAT 95% CL upper limit vs. the ΔC-Stat values for our spectroscopic subsample. The long and short dashed lines represent the line of equality between the LAT upper limits and the expected LAT flux and the ΔC-Stat value representing a 3σ fit improvement, respectively. The bursts for which a spectral break is statistically preferred have the most severe discrepancies between the GBM-only extrapolations and the LAT upper limits.

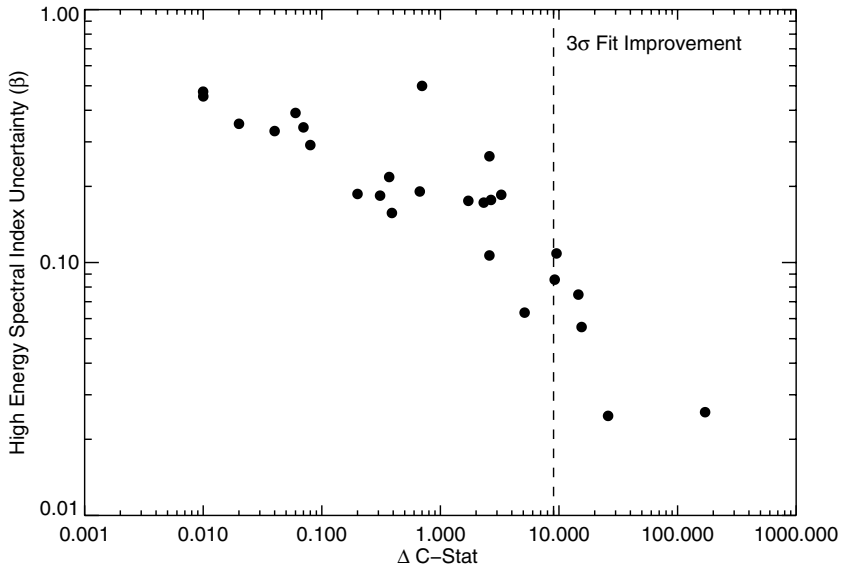

Figure 10. 1σ symmetric uncertainty in the high-energy spectral index found from fits to the GBM data alone vs. the ΔC-Stat values for our spectroscopic subsample. The bursts for which a spectral break is statistically preferred also have the smallest uncertainties in their GBM-only β values.

follows from the threshold condition for e^+e^- pair production, when both the incident and target photons are at the maximum observed energy.

If a high-energy γ-ray photon with energy E and the observed broadband photon emission originate from the same physical region, and if we assume the photons are quasi-isotropic in the comoving frame, then the $\gamma\gamma \rightarrow e^+e^-$ pair production optical depth can be written as

$$\tau_{\gamma\gamma}(E) = \frac{3}{4}\frac{\sigma_T d_L^2}{t_v \Gamma}\frac{m_e^4 c^6}{E^2(1+z)^3}\int_{\frac{m_e^2 c^4 \Gamma}{E(1+z)}}^{\infty}\frac{d\epsilon'}{\epsilon'^2}n \times\left(\frac{\epsilon'\Gamma}{1+z}\right)\varphi\left[\frac{\epsilon' E(1+z)}{\Gamma}\right]. \quad (1)$$

Here, $n(\epsilon)$ is the observed photon spectrum, ϵ is the target photon energy, ϵ' is the target photon energy in the comoving frame of the emitting plasma, d_L is the luminosity distance, t_v is the γ-ray flux variability timescale, and σ_T is the Thomson cross-section. The function $\varphi[\epsilon' E(1+z)/\Gamma]$ is defined by Gould & Schréder (1967) and Brown et al. (1973). The value of $\Gamma_{\gamma\gamma,\min}$ follows from the condition $\tau_{\gamma\gamma}(E_{\max}) = 1$. This single-zone model, in which the spatial and temporal dependencies of $\tau_{\gamma\gamma}$ have been averaged out, has been the technique used to measure the reported values of $\Gamma_{\gamma\gamma,\min}$ for the LAT detections of GRBs 080916C, 090510, and 09092B in Abdo et al. (2009b), Ackermann et al. (2010), and Abdo et al. (2009a), respectively. It is important to note that these single-zone models may provide overestimated Lorentz factors compared to time-dependent multi-zone models that consider the possibility of multiple emitting regions and that take into account the time variability of $\tau_{\gamma\gamma}$. For a discussion of single and multi-zone models, see Zou et al. (2011).

A direct estimate of the bulk Lorentz factor Γ, as opposed to a minimum value, of the GRB jet can be made based on evidence of a cutoff in the spectral fits that are attributed to $\gamma\gamma$

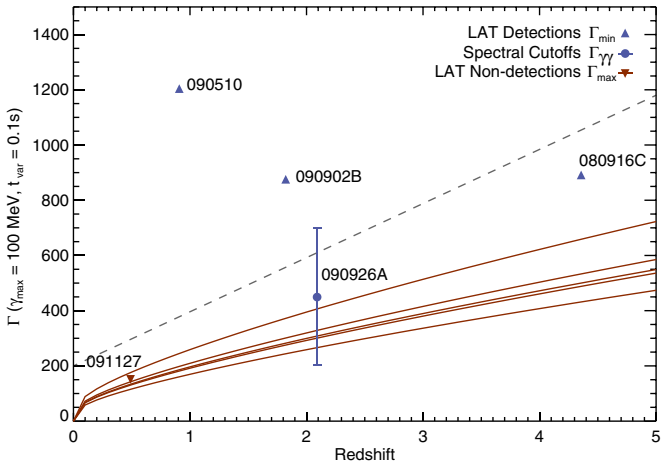

Figure 11. Γ_{max} values for the six GRBs in our sample with evidence for spectral breaks compared to the Γ_{min} values for the brightest LAT-detected GRBs. The allowed range of Γ_{max} values for $0 < z < 5$ all lie well below the Γ_{min} values of the LAT-detected GRBs. The Γ estimate for GRB 090926A from Abdo et al. (2011) is shown as the filled blue circle. The gray dashed line demarcates the self-consistency line where the condition that $\Gamma \leqslant E_{max}(1+z)/m_e c^2$ is violated. The range of Lorentz factors obtained through the use of single-zone and time-dependent models places GRB 090926A between the LAT-detected and LAT dark GRBs.

(A color version of this figure is available in the online journal.)

attenuation, such as has been reported for GRB 090926A in Abdo et al. (2011).

In the case of the six GRBs that we consider here for which no direct evidence for a spectral cutoff is otherwise detected, we use our upper limits to calculate a maximum bulk Lorentz factor $\Gamma_{\gamma\gamma,max}$ from the condition $\tau_{\gamma\gamma}(E_{UL}) = 1$. To do so, we use the Band function fit to the GBM and LAT data and set $E_{UL} = 100$ MeV. We also assume a variability timescale of $t_v = 0.1$ s, which we believe represents a conservative estimate of t_v given the ubiquity of millisecond variability in BATSE-detected GRBs (Walker et al. 2000) as well as the short timescales observed in other LAT-detected GRBs (Ackermann et al. 2010).

We note that if the cutoff energy due to intrinsic pair opacity is small enough, $E_{cutoff} < m_e c^2 \Gamma/(1+z)$, then the Thomson optical depth of the pairs that are produced in the emitting region is $\tau_{T,e^{\pm}} > 1$ (Lithwick & Sari 2001; Abdo et al. 2009a). This should affect both the observed spectrum, thermalizing it for a large enough optical depth, and light curve, eliminating short timescale variability. For $E_{cutoff} = 100$ MeV, this condition is nearly violated at $z \lesssim 1.0$, therefore a much lower cutoff energy would be hard to reconcile with an intrinsic pair opacity origin for GRBs at low redshift.

The resulting $\Gamma_{\gamma\gamma,min}$ and $\Gamma_{\gamma\gamma,max}$ values for previously reported LAT detections and from the upper limits presented here are shown in Figure 11. Since the Lorentz factor calculation depends on the redshift, which is unknown for the majority of GBM-detected bursts, we have plotted the $\Gamma_{\gamma\gamma,max}$ values as a function of the redshift (red lines). One GRB in our spectroscopic subsample, GRB 091127, has a measured redshift which allows us to constrain the burst's Γ_{max} value. Using a redshift of $z = 0.490$ (Cucchiara et al. 2009) and $E_{UL} \sim 100$ MeV, we calculate a relatively small bulk Lorentz factor of $\Gamma_{max} \sim 155$. Using the measurements of E_{UL} for these GRBs provides a relatively narrow distribution of Γ_{max} that range from $50 < \Gamma_{max} < 300$ at $z = 1$ to $400 < \Gamma_{\gamma\gamma,max} < 640$ at $z = 4$. These values stand in stark contrast to the LAT-detected GRBs for which $\Gamma_{\gamma\gamma,min}$ was measured, all of which have $\Gamma_{\gamma\gamma,min} > 800$. Our results are consistent with those presented by Beniamini et al. (2011) and Guetta et al. (2011), who used the non-detection of a smaller sample of GBM-detected bursts to also infer the $\Gamma_{\gamma\gamma,max}$ of the emitting region.

The detection of spectral curvature by the LAT in the spectrum of GRB 090926 provides a case that appears to bridge the LAT detected and non-detected samples. The estimate of Γ of 200–700 presented in Abdo et al. (2011) reflects the systematic differences between Lorentz factors obtained through the use of time-dependent models by Granot et al. (2008) which yield systematic differences in $\tau_{\gamma\gamma}$ and the inferred Γ when compared to the simple single-zone model used above. Granot et al. (2008), and more recently Hascoët et al. (2012), have shown that such time-dependent models, which include the temporal evolution of $\tau_{\gamma\gamma}$ during the emission period, can yield inferred Γ estimates that are reduced by a factor of 2–3 compared to estimates made using single-zone models. In the context of these time-dependent model, the $\Gamma_{\gamma\gamma,min}$ and $\Gamma_{\gamma\gamma,max}$ presented in Figure 11 would all be systematically overestimated by a factor of 2–3, but the dichotomy between the LAT detected and LAT non-detected GRBs would persist since all Γ estimates would be effected by the same correction.

Note that the gray dashed line in Figure 11 demarcates the self-consistency line where the condition that $\Gamma \leqslant E_{max}(1+z)/m_e c^2$ is violated, implying an incorrect determination of $\tau_{\gamma\gamma}$, for the bursts with no detected emission above $E_{max} = 100$ MeV. None of the bursts in our spectroscopic subsample violate this condition at any redshift for the choice of $E_{cutoff} = 100$ MeV.

6. DISCUSSION

The upper limits presented above place stringent constraints on the high-energy emission from GRBs detected by the GBM. Of the 620 bursts detected by the GBM from 2008 August 4 to 2011 January 1, 46% were within the LAT FOV. There is evidence for high-energy emission >100 MeV in the LAT energy range for 23 GRBs, representing 8% of the entire GBM sample observed by the LAT. This is significantly less than the pre-launch estimate of one detection per month that produces at least 100 counts above 100 MeV (Band et al. 2009).

The results of our joint GBM and LAT spectral fits show that both softer high-energy power-law spectra and spectral breaks likely account for the lower-than-expected number of LAT-detected GRBs. For the 24 bursts in our spectroscopic subsample where a spectral break is not statistically justified, the β values from the joint fits are systematically softer than the values found from fitting the GBM data alone. This may indicate that the high-energy spectral index for the Band model may in fact be softer than that deduced from measurements made by previous missions, such as BATSE, which had a much narrower energy range compared to the combined coverage of the GBM and LAT. The GBM+LAT β distribution shown in Figure 7 appears to exclude the harder spectra found from fits made with just the lower energy BATSE or GBM data. In fact, we find no cases of spectra with $\beta > -2.0$, which would otherwise result in a divergent energy flux at high energies.

The results of our extrapolation of GBM fits into the LAT energy range are roughly consistent with similar conclusions drawn by Beniamini et al. (2011) and Guetta et al. (2011) who perform a variation of the upper limit analysis presented here on a smaller sample of GBM-detected bursts and conclude that there are significant differences between expected flux in the LAT energy range and their calculated LAT upper limits.

Although, we emphasize that a simple extrapolation of spectral fits to GBM data is not a sufficient method of estimating the expected flux in the LAT energy range. Inclusion of the LAT upper limits in the spectral fit can drastically change the best-fit parameters, beyond the statistical error obtained by fitting GBM data alone, in order to accommodate the LAT upper limits. This point represents a major difference between the depth and precision of our analysis and that presented by Beniamini et al. (2011) and Guetta et al. (2011).

Our results clearly show that in many GRBs there must be a softening in the Band component at high energies. If the Band high-energy photon index (beta) reflects the underlying slope of the relativistic electron energy distribution, as assumed in most models, then this could imply a softening of their energy distribution, which represents a deviation from a power law (namely, a convex energy spectrum). It is possible that this could be associated with a cooling break of index $\Delta\beta = -1/2$ in some bursts, but our step-function protocol here might suggest a more severe steepening is present. Alternatively, this might be caused by intrinsic pair production in the source, in which case it does not reflect any deviation from a power law of the electron energy distribution. Typically, such breaks are more profound than cooling ones corresponding to $\Delta\beta < -1$ (e.g., Baring 2006; Granot et al. 2008). Moreover, if the MeV component is synchrotron (or first-order synchrotron self-Compton, SSC) then the first (or second) order SSC is expected to contribute at LAT energies, and our upper limits imply that it must be suppressed. One way of achieving this is through the same intrinsic opacity to pair production that can attenuate the Band component, if this is indeed the cause of the suppression in the LAT window. Alternatively, a small relativistic electron to magnetic energy density ratio in the emitting region could lead to a small Compton y-parameter ($Y \sim \epsilon_e/\epsilon_B \lesssim 0.1$) thus suppressing the SSC component/s; this is akin to parameter space invoked for SSC models of low gamma-ray flux blazars. However, this would imply a low radiative efficiency ($\lesssim 0.1\epsilon_B < 0.1$), and would be particularly problematic if the MeV component is interpreted as first-order SSC. In addition, it would still require an independent mechanism for suppressing or attenuating the Band component above around 30 MeV, thus making such a scenario even less compelling. Altogether, our results put strong constraints on synchrotron and SSC models and are consistent with conclusions drawn by Beniamini et al. (2011) and Guetta et al. (2011) who performed a variation of the upper limit analysis presented here on a smaller sample of GBM-detected bursts.

The detection of softer β values also provides support for continuum models with multiple components, which have been used to describe novel spectral features detected by the GBM and LAT. Recent work on bright GRBs by Guiriec et al. (2011) suggests that although the Band function represents many GRB spectra very well in a limited energy range, it is sometimes possible to discern, even in this limited energy range, contributions such as thermal components in addition to the presumably non-thermal synchrotron emission represented by the Band function. The addition of such components to a Band function has the effect of modifying the parameter values, in the case of GRB 100724B rising $E_{\rm pk}$ and softening β (Guiriec et al. 2011). While these more complex models are not statistically favored in most GRBs due to low photon statistics, their successful fits to some GRBs indicate that the representation of GRB emission by a Band function may be inadequate and lead to overestimates of fluxes when extrapolated to GeV energies. Because the Band function was developed to represent GRB spectra rather than to parameterize a physical model, it is difficult to decouple physical components from this empirical function, which probably incompletely describes elements of multiple physical phenomena. Additionally, the superposition of Band functions does not necessarily produce a Band function, so the presence of spectral evolution means that any extrapolation to higher energies from flux-averaged spectra may not be representative of the emission throughout the entire GRB emission period.

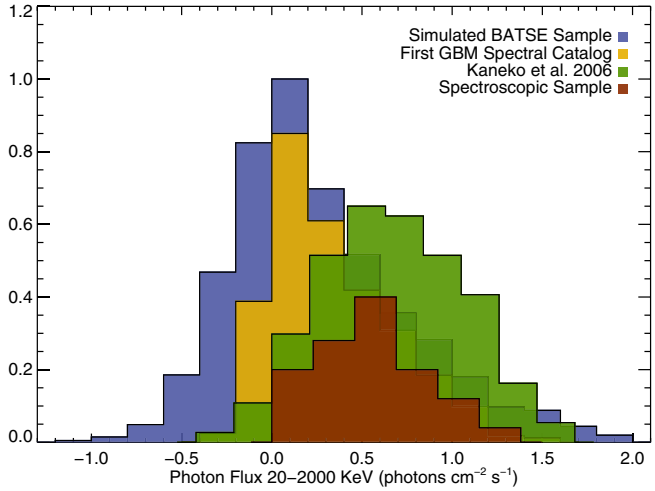

Figure 12. Normalized distribution of the time-integrated photon flux as determined through our fits to GBM data for the spectroscopic subsample (red), the bursts in the bright BATSE catalog presented in Kaneko et al. (2006; green), the bursts that appear in the first GBM spectral catalog (gold), and a sample of simulated BATSE bursts (blue) using the spectral parameter distributions given in Preece et al. (2000). The resulting distributions show that our spectroscopic subsample is consistent with being drawn from the distribution of the brightest bursts detected by the GBM and BATSE.

(A color version of this figure is available in the online journal.)

Granot et al. (2008) have shown that even when integrating over a single spike in a light curve there is a steepening to a softer power law rather than an exponential cutoff. This is due to the high-energy power law arising from the sum of instantaneous spectra with an exponential cutoff whose break energy evolves with time. Likewise, Hascoët et al. (2012) have shown that the effect of averaging a time variable opacity cutoff would be manifested as a steepening in the power-law index of the high-energy spectral slope rather than as a sharp cutoff in the spectrum. Likewise, Baring (2006) has shown that skin-depth effects tend to smear out exponential attenuation when the source and target photons originate in the same volume, resulting in a similar effect. Such considerations could explain the softer β values found when fitting both the GBM and LAT data, even in cases where a spectral break was not statistically preferred. Detailed time resolved spectroscopy of bright GBM-detected GRBs should be able to discriminate between such pair opacity effects, intrinsically steeper high-energy spectra, or the more complex continuum models discussed above β (Guiriec et al. 2011).

The bursts in our spectroscopic subsample were chosen specifically because they were among the brightest bursts detected by the BGO and yet had no appreciable signal in the LAT. This makes them good candidates to examine for evidence of spectral breaks, but they may also form a biased data set. In order to understand how representative these bursts are of the general GRB population, we plot in Figure 12 the distribution of the time-averaged photon flux as determined from fits to

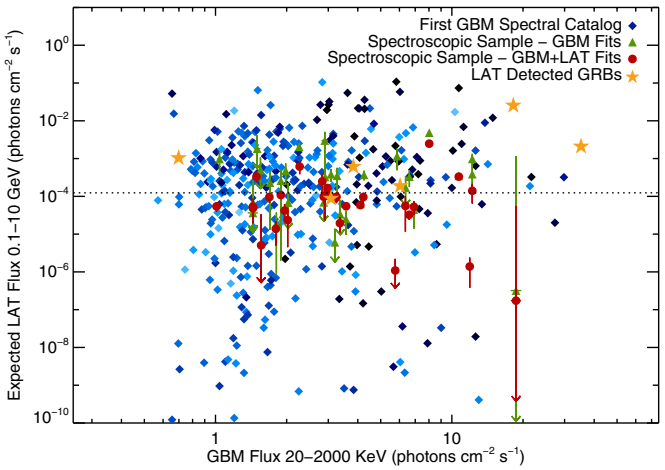

Figure 13. Band function model fluxes in the 0.1–10 GeV energy range vs. the 0.02–2 MeV energy range for various measure and simulated data. The gold stars represent the six *Fermi* bursts that were detected by the LAT during the first 18 months that can be well fit by a Band function model; the green circles represent spectral fits to GBM data for the 30 bright BGO bursts in our spectroscopic subsample; the red circles represent spectral fits to GBM and LAT data for the same 30 GRBs; and the blue circles represent bursts that appear in the first GBM spectral catalog for which a Band spectral model could be fit. The color gradient in the GBM sample represents the burst's T90 duration.

(A color version of this figure is available in the online journal.)

GBM data for bursts in our spectroscopic subsample (red), the bursts which appear in the first GBM spectral catalog (gold), the bursts in the bright BATSE catalog presented in Kaneko et al. (2006; green), and a sample of simulated BATSE bursts (blue) using the spectral parameter distributions given in Preece et al. (2000). The resulting distributions show that the spectroscopic subsample is consistent with being drawn from the distribution of the brightest bursts detected by BATSE.

We extend this analysis in Figure 13, where we plot the expected 0.1–10 GeV LAT photon flux versus the 20–2000 keV photon flux for our spectroscopic sample using spectral parameters from the GBM-only fits (green) and from the joint GBM–LAT fits (red), along with the bursts from the first GBM spectral catalog which were in the LAT FOV (blue). The color gradient in the GBM sample represents the burst's duration, with darker (blue) symbols representing shorter duration bursts. In addition, we have plotted the six LAT-detected bursts (gold) that had spectra that could be fit with a single Band function (i.e., we excluded bursts with extra high-energy components). The dashed line represents the median T100 upper limit. The green data points demonstrate how fits to the GBM data without the inclusion of the LAT data yield spectral parameters that overpredict the flux in the LAT energy range, which can be seen by the number of bursts in our spectroscopic subsample that fall above the median upper limit values. The red data points represent the predicted LAT flux for the same GRBs using spectral parameters determined through fits to both the GBM and LAT data. Roughly 50% of the bursts from the GBM spectral catalog fall above the median T100 upper limit. This would imply that a large fraction of bright GBM-detected bursts would have been detectable by the LAT assuming a direct extrapolation of their high-energy spectra. Therefore, we conclude that intrinsic spectral breaks and/or softer-than-measured high-energy spectra must be fairly common in the GRB population in order to explain the lack of LAT-detected GRBs.

Despite the unknown distances to all but one of the GRBs in our spectroscopic subsample, the allowed range of $\Gamma_{\gamma\gamma,\max}$ values for $0 < z < 5$ all lie well below $\Gamma_{\gamma\gamma,\max} \sim 720$. This range of $\Gamma_{\gamma\gamma,\max}$ for the relativistic outflow contrasts with the minimum Lorentz factors that have been calculated for the bright, LAT-detected GRBs using their highest detected photons. For GRB 080916C, GRB 090510, and GRB 09092B, the estimated lower limits for the Lorentz factors were found to be 887, 1200, and 867 when using single zone models, respectively. Therefore, measurements of $\Gamma_{\gamma\gamma,\min}$ and $\Gamma_{\gamma\gamma,\max}$ from both LAT detections and non-detections reveal a wide distribution in the bulk Lorentz factor of GRB outflows, with a potential range of over $\sim$10.

As discussed above, these estimates of $\Gamma_{\gamma\gamma,\min}$ and $\Gamma_{\gamma\gamma,\max}$ have been calculated using simple single-zone models, which may provide overestimated values compared to time-dependent multi-zone models that take into account the time variability of $\tau_{\gamma\gamma}$. In such a scenario, our estimates of the $\Gamma_{\gamma\gamma,\min}$ and $\Gamma_{\gamma\gamma,\max}$ would need to be rescaled downward by a factor of 2–3 (Granot et al. 2008; Zou et al. 2011; Hascoët et al. 2012), but the large difference between the LAT detected and non-detected GRBs would remain.

The *Fermi* LAT Collaboration acknowledges generous ongoing support from a number of agencies and institutes that have supported both the development and the operation of the LAT as well as scientific data analysis. These include the National Aeronautics and Space Administration and the Department of Energy in the United States, the Commissariat à l'Energie Atomique and the Centre National de la Recherche Scientifique/Institut National de Physique Nucléaire et de Physique des Particules in France, the Agenzia Spaziale Italiana and the Istituto Nazionale di Fisica Nucleare in Italy, the Ministry of Education, Culture, Sports, Science and Technology (MEXT), High-energy Accelerator Research Organization (KEK) and Japan Aerospace Exploration Agency (JAXA) in Japan, and the K. A. Wallenberg Foundation, the Swedish Research Council, and the Swedish National Space Board in Sweden.

Additional support for science analysis during the operations phase is gratefully acknowledged from the Istituto Nazionale di Astrofisica in Italy and the Centre National d'Études Spatiales in France.

The *Fermi* GBM Collaboration acknowledges support for GBM development, operations, and data analysis from NASA in the US and BMWi/DLR in Germany.

REFERENCES

Abdo, A. A., Ackermann, M., Ajello, M., et al. 2009a, ApJ, 706, L138
Abdo, A. A., Ackermann, M., Ajello, M., et al. 2010, ApJ, 712, 558
Abdo, A. A., Ackermann, M., Arimoto, M., et al. 2009b, Science, 323, 1688
Abdo, A. A., Ackermann, M., Asano, K., et al. 2009c, ApJ, 707, 580
Abdo, A. A., Ajello, M., Asano, K., et al. 2011, ApJ, 729, 114
Ackermann, M., Ajello, M., Asano, K., et al. 2011, ApJ, 729, 114
Ackermann, M., Asano, K., Atwood, W. B., et al. 2010, ApJ, 716, 1178
Amsler, C., Doser, M., Antonelli, M., et al. 2008, Phys. Lett. B, 667, 1
Atwood, W. B., Abdo, A. A., Ackermann, M., et al. 2009, ApJ, 697, 1071
Band, D., Matteson, J., Ford, L., et al. 1993, ApJ, 413, 281
Band, D. L., Axelsson, M., Baldini, L., et al. 2009, ApJ, 701, 1673
Baring, M. G. 2006, ApJ, 650, 1004
Beniamini, P., Guetta, D., Nakar, E., & Piran, T. 2011, MNRAS, 416, 3089
Bissaldi, E., von Kienlin, A., Kouveliotou, C., et al. 2011, ApJ, 733, 97
Brown, R. W., Mikaelian, K. O., & Gould, R. J. 1973, Astrophys. Lett., 14, 203
Cash, W. 1976, A&A, 52, 307
Connaughton, V. 2011, GCN, 11574, 1C
Cucchiara, A., Fox, D., Levan, A., & Tanvir, N. 2009, GRB Coordinates Network, 10202, 1
Del Monte, E., Barbiellini, G., Donnarumma, I., et al. 2011, A&A, 535, A120
Fan, Y., & Piran, T. 2008, Front. Phys. China, 3, 306

Gehrels, N., Chincarini, G., Giommi, P., et al. 2004, ApJ, 611, 1005
Goldstein, A., Burgess, J. M., Preece, R. D., et al. 2012, ApJS, 199, 19
González, M. M., Dingus, B. L., Kaneko, Y., et al. 2003, Nature, 424, 749
Gould, R. J., & Schréder, G. P. 1967, Phys. Rev., 155, 1408
Granot, J., Cohen-Tanugi, J., & do Couto e Silva, E. 2008, ApJ, 677, 92
Guetta, D., Pian, E., & Waxman, E. 2011, A&A, 525, A53
Guiriec, S., Connaughton, V., Briggs, M. S., et al. 2011, ApJ, 727, L33
Hascoët, R., Daigne, F., Mochkovitch, R., & Vennin, V. 2012, MNRAS, 421, 525
Helene, O. 1983, Nucl. Instrum. Methods Phys. Res., 212, 319
Hurley, K., Dingus, B. L., Mukherjee, R., et al. 1994, Nature, 372, 652
Jackson, B., Scargle, J., Barnes, D., et al. 2005, IEEE Signal Process. Lett., 12, 105
Kaneko, Y., Preece, R. D., Briggs, M. S., et al. 2006, ApJS, 166, 298
Kouveliotou, C., Preece, R., Bhat, N., et al. 1994, ApJ, 422, L59
Kraft, R. P., Burrows, D. N., & Nousek, J. A. 1991, ApJ, 374, 344
Lithwick, Y., & Sari, R. 2001, ApJ, 555, 540
Mattox, J. R., Bertsch, D. L., Chiang, J., et al. 1996, ApJ, 461, 396
McBreen, S., Krühler, T., Rau, A., et al. 2010, A&A, 516, A71
Meegan, C., Lichti, G., Bhat, P. N., et al. 2009, ApJ, 702, 791
Preece, R. D., Briggs, M. S., Mallozzi, R. S., et al. 2000, ApJS, 126, 19
Razzaque, S., Mészáros, P., & Zhang, B. 2004, ApJ, 613, 1072
Sommer, M., Bertsch, D. L., Dingus, B. L., et al. 1994, ApJ, 422, L63
Walker, K. C., Schaefer, B. E., & Fenimore, E. E. 2000, ApJ, 537, 264
Zou, Y.-C., Fan, Y.-Z., & Piran, T. 2011, ApJ, 726, L2